

Multifractal-enriched mobility edges and emergent quantum phases in Rydberg atomic arrays

Shan-Zhong Li,^{1,2} Yi-Cai Zhang,³ Yucheng Wang,⁴ Shanchao Zhang,^{1,2,5} Shi-Liang Zhu,^{1,2,5,*} and Zhi Li^{1,2,†}

¹Key Laboratory of Atomic and Subatomic Structure and Quantum Control (Ministry of Education),
Guangdong Basic Research Center of Excellence for Structure and Fundamental Interactions of Matter,
School of Physics, South China Normal University, Guangzhou 510006, China

²Guangdong Provincial Key Laboratory of Quantum Engineering and Quantum Materials,
Guangdong-Hong Kong Joint Laboratory of Quantum Matter,
Frontier Research Institute for Physics, South China Normal University, Guangzhou 510006, China

³School of Physics and Materials Science, Guangzhou University, Guangzhou 510006, China

⁴Shenzhen Institute for Quantum Science and Engineering,

Southern University of Science and Technology, Shenzhen 518055, China

⁵Quantum Science Center of Guangdong-Hong Kong-Macao Greater Bay Area, Shenzhen, China

Anderson localization describes disorder-induced phase transitions, distinguishing between localized and extended states. In quasiperiodic systems, a third multifractal state emerges, characterized by unique energy and wave functions. However, the corresponding multifractal-enriched mobility edges and three-state-coexisting quantum phases have yet to be experimentally detected. In this work, we propose exactly-solvable one-dimensional quasiperiodic lattice models that simultaneously host three-state-coexisting quantum phases, with their phase boundaries analytically derived via Avila's global theorem. Furthermore, we propose experimental protocols via Rydberg atom arrays to realize these states. Notably, we demonstrate a spectroscopic technique capable of measuring inverse participation ratios across real-space and dual-space domains, enabling simultaneous characterization of localized, extended, and multifractal quantum phases in systems with up to tens of qubits. Our work opens new avenues for the experimental exploration of Anderson localization and multifractal states in artificial quantum systems.

Introduction.— Anderson localization elucidates a fundamental principle concerning how disorder induces a metal-insulator phase transition [1], which separates phases characterized by localized and extended states. Furthermore, three-dimensional periodic systems or even one-dimensional quasiperiodic lattices [2] may exhibit phases where extended and localized states coexist, with a mobility edge (ME) distinguishing between them [3]. Additionally, in quasiperiodic systems, a third fundamental state known as multifractal state emerges [4, 5]. The energy level statistics [6, 7], wave function distributions [8, 9], and dynamical properties [10, 11] of the multifractal state significantly differ from those of localized and extended states. The discovery of multifractal states has significantly broadened our understanding of Anderson localization. For instance, recent studies indicate that the multifractal state may enhance the superconducting transition temperature [12–16].

Recent research has focused on identifying multifractal-enriched mobility edges (MMEs), which serve as boundaries separating multifractal states from either extended or localized states [17–29]. However, much of the progress in understanding MMEs has relied on numerical analyses, often involving tedious scaling assessments [18–24]. Recently, several approaches have been proposed to derive exact expressions for MMEs [25–32]. Despite significant efforts in studying MMEs [17–29, 31–33], a fundamental question remains unanswered: Is there a universal platform capable of generating all types of MMEs and enabling the explo-

ration of all possible multi-state coexisting quantum phases? Furthermore, while these states have been extensively investigated theoretically using LEs and IPRs [24–29, 32–51], these definitive indicators have yet to be experimentally observed. This raises a critical question: How can we experimentally realize all MMEs and establish a practical protocol for their detection?

In this Letter, we address these challenges by introducing a class of exactly solvable models that can be readily realized using Rydberg atom arrays. Specifically, we present a class of exactly solvable one-dimensional quasiperiodic flat band lattices, which host MMEs and emergent quantum phases. All phase boundaries in these systems are analytically determined using Avila's global theorem [52], thereby circumventing the need for the tedious scaling analyses typically required in disordered systems [17–24]. Furthermore, we demonstrate that these models can be implemented in artificial quantum systems, such as superconducting quantum circuits and Rydberg atom arrays, and we provide a detailed realization scheme for Rydberg atom arrays. Remarkably, the key features of localized, extended, and multifractal states can be distinguished in systems with up to tens of qubits compared to several hundreds of qubits currently controllable in many research groups [53–55]. The critical problem in detecting MMEs lies in distinguishing extended states from multifractal regimes. While IPRs have been extensively employed in theoretical and numerical studies of Anderson localization and mobility edges [21, 25–29, 31, 34–51], experimental observation of MMEs

via IPR remains unexplored. Inspired by the method outlined in Ref. [31], we develop a spectroscopic technique that simultaneously measures IPRs in real-space and dual-space domains, thereby resolving this problem.

The Diamond Lattice Model and Main Results.—We analytically demonstrate that MMEs can arise in a class of flat-band models featuring partially quasiperiodic modulation (see Supplementary Materials (SM) [56]). As a representative example, we here utilize a diamond lattice [57] shown in Fig. 1(a) to illustrate our ideas, and the Hamiltonian of this model reads

$$H_D = \sum_{n=1}^N (Ja_n^\dagger b_n + Ja_n^\dagger c_n + tb_n^\dagger c_n + \text{H.c.}) + \sum_{n=1}^{N-1} (Jb_n^\dagger a_{n+1} + Jc_n^\dagger a_{n+1} + \text{H.c.}) + \sum_{n=1}^N V_n c_n^\dagger c_n, \quad (1)$$

where a_n (a_n^\dagger), b_n (b_n^\dagger), and c_n (c_n^\dagger) are the annihilation (creation) operators corresponding to sublattices A, B, and C in the n -th primitive cell, respectively. The quantities J and t denote the hopping strengths between the A and B/C sublattices and between the B and C sublattices, respectively. Here, N denotes the total number of primitive cells. A quasiperiodic potential, defined as $V_n = 2\lambda \cos(2\pi\alpha n + \theta)$, is applied solely to sublattice C, where λ , α , and θ represent the strength of the quasiperiodic potential, an irrational number, and a phase offset, respectively. When $\lambda = 0$, Hamiltonian (1) showcases a perfect flat band characterized by $E_k = -t$ along with two dispersive bands given by $E_k = (t \pm \sqrt{16J^2 \cos(k) + 16J^2 + t^2})/2$ [57].

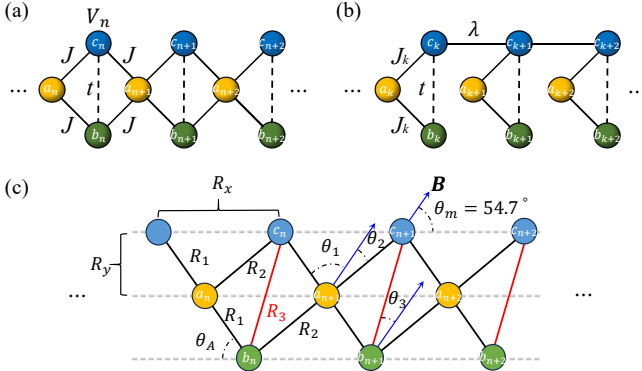


FIG. 1. The diamond lattice model represented in (a) lattice space, (b) dual space, (c) and its experimental implementation with Rydberg atomic array.

To accurately derive the MEs of Hamiltonian (1), we employ a dual space as an auxiliary framework. By applying the dual transformations $a_n = \frac{1}{\sqrt{N}} \sum_k a_k e^{-i2\pi\alpha kn}$, $b_n = \frac{1}{\sqrt{N}} \sum_k b_k e^{-i2\pi\alpha kn}$, and $c_n = \frac{1}{\sqrt{N}} \sum_k c_k e^{-i2\pi\alpha kn}$ for $\theta = 0$, we can derive the corre-

sponding Hamiltonian in dual space:

$$H_K = \sum_{k=1}^N (J_k a_k^\dagger b_k + J_k a_k^\dagger c_k + \text{H.c.}) + \sum_{k=1}^N (tb_k^\dagger c_k + \text{H.c.}) + \sum_{k=1}^{N-1} (\lambda c_{k+1}^\dagger c_k + \text{H.c.}), \quad (2)$$

where $J_k = J + J e^{(i2\pi\alpha k)}$. The geometric structure (refer to Fig. 1(b)) illustrates that the system operates as an extended Fano defect quasiperiodic lattice in dual space [57]. For the purpose of numerical calculations, we set $J = 1$ as the energy unit and impose periodic boundary conditions. The additional parameters are $\theta = 0$ and $\alpha = \lim_{m \rightarrow \infty} \frac{F_{m-1}}{F_m} = (\sqrt{5} - 1)/2$, where F_m denotes the m -th Fibonacci number. In finite-size studies, we specify the system size as $N = F_m$ and $\alpha = F_{m-1}/F_m$ to maintain accurate periodic boundary conditions. The MEs of Hamiltonian (1) can be categorized into two scenarios: $t < 2$ and $t \geq 2$. Given the similarity of outcomes in both cases, we present only the results for $t < 2$ in the main text (see SM [56] for the $t \geq 2$ case).

The primary findings of our analysis indicate that a comprehensive set of MMEs and all possible coexisting quantum phases can emerge within a class of flat-band models featuring partially quasiperiodic modulations. Furthermore, these predictions are readily demonstrable in current artificial quantum systems.

The universal analytical expressions for the MMEs and the potential quantum phases of model (1) are consolidated in Table I. To facilitate comprehension of the universal expressions presented in this table, we depict results for a specific case in Fig. 2, which delineates three distinct regions. In the region $\lambda \leq 1$, we identify two types of MEs: one being a traditional ME that distinguishes between localized and extended states, and the other an MME that differentiates multifractal from extended states. In the region $1 < \lambda < 3$, we observe three types of MEs: one separating localized and extended states, another MME separating multifractal and extended states, and the third MME distinguishing multifractal from localized states. Finally, in the region $\lambda \geq 3$, only a single type of MME exists, effectively separating localized states from multifractal states, while the corresponding multi-state coexisting quantum phases also arise.

Analytical expressions of the LEs.— In Anderson localization, the LE characterizes the inverse localization length of wavefunctions: A positive LE signifies exponential spatial decay (localized states), while a vanishing LE indicates extended states. The mobility edge, separating these phases, corresponds to critical LEs. We now demonstrate that the LEs for the diamond lattice model can be analytically derived using Avila's global theory [52]. The $\gamma_{R(K)}$ defined as the LE of the eigenstate associated with the eigenvalue E in lattice (dual)

TABLE I. MMEs and emergent quantum phases of model (1) under the condition of $t < 2$

Disorder strength	$\lambda \leq 2 - t$		$2 - t < \lambda < 2 + t$			$\lambda \geq 2 + t$
Exact MMEs ($E_c =$)	$\pm \frac{1}{\lambda} \pm \sqrt{\frac{1}{\lambda^2} \pm \frac{2t}{\lambda} + 2}$	$\pm \lambda - t$	$\frac{1}{\lambda} + \sqrt{\frac{1}{\lambda^2} + \frac{2t}{\lambda} + 2}$	$\lambda - t$	-2	± 2
Separated states	Ext.* and Loc.	Ext. and Mul.	Ext. and Loc.	Ext. and Mul.	Ext. and Mul.	Loc. and Mul.
Quantum phases	Ext.+Mul.; Ext.+Mul.+Loc.		Ext.+Mul.+Loc.			Loc.+Mul.

*Ext.=Extended states; Loc.=Localized states; Mul.=Multifractal states.

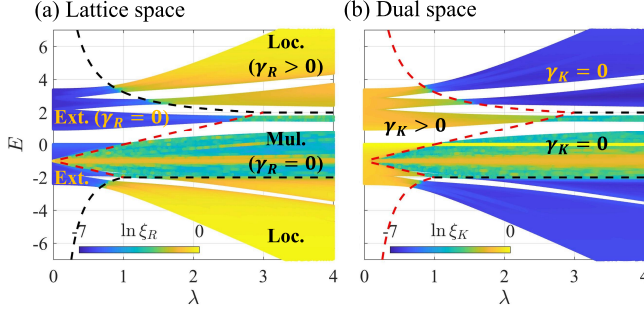


FIG. 2. Phase diagram of the diamond lattice model. (a) The lattice space IPR ξ_R and (b) the dual space IPR ξ_K as functions of potential strength λ and energy E . The phase boundaries, marked by dashed lines, are determined from the critical energies that have been exactly solved. The parameters $N = 377$ and $t = 1$.

space can be obtained from

$$\gamma_{R(K)} = \lim_{N \rightarrow \infty} \frac{1}{N} \ln \left\| \prod_{n(k)=1}^N T_{n(k)} \right\|, \quad (3)$$

where $\|\cdot\|$ denotes the matrix norm, and $T_{n(k)}$ represents the transfer matrix. The properties of the LEs are summarized in Table II [28].

The LE in lattice space is mathematically determined by the eigenequation of the Hamiltonian (1): $\psi_{b,n-1} + \psi_{c,n-1} + \psi_{b,n} + \psi_{c,n} = E\psi_{a,n}$, $\psi_{a,n+1} + \psi_{a,n} + t\psi_{c,n} = E\psi_{b,n}$, $\psi_{a,n+1} + \psi_{a,n} + t\psi_{b,n} + V_n\psi_{c,n} = E\psi_{c,n}$. By simplifying the equations, one can get

$$\begin{aligned} \psi_{c,n+1} = & \frac{E^3 - (E^2 - 2)V_n - t^2E - 4(E+t)}{2(E+t) - V_{n+1}} \psi_{c,n} \\ & - \frac{2(E+t) - V_{n-1}}{2(E+t) - V_{n+1}} \psi_{c,n-1}. \end{aligned} \quad (4)$$

By extracting coefficients, one can obtain the transfer matrix as $T_n = A_n B_n$, where $A_n = 1/M_{n+1}$ and

$$B_n = \begin{pmatrix} E^3 - (E^2 - 2)V_n - t^2E - 4(E+t) & -M_{n-1} \\ M_{n+1} & 0 \end{pmatrix}$$

with $M_n = 2(E+t) - V_n$. Utilizing Avila's global theory [52], we derive analytical expressions for the LEs in terms of the eigenvalue E in lattice space. Similarly, we

TABLE II. Key indicators of states' localization feature

States	LEs	IPRs
Ext.	$\gamma_R = 0$ & $\gamma_K > 0$	$\xi_R \sim 1/3N$ & $\xi_K(E) \sim \mathcal{O}(1)$
Loc.	$\gamma_R > 0$ & $\gamma_K = 0$	$\xi_R \sim \mathcal{O}(1)$ & $\xi_K \sim 1/3N$
Mul.	$\gamma_R = 0$ & $\gamma_K = 0$	$1/3N < \xi_R \approx \xi_K < \mathcal{O}(1)$

can also obtain the analytical LEs in dual space. The complete expressions for the LEs can be written as

$$(\gamma_R, \gamma_K) = \begin{cases} (\gamma_{R,1}, \gamma_{K,1}), & |E+t| > \lambda \text{ \& \; } |E^2 - 2| > 2, \\ (\gamma_{R,2}, 0), & |E+t| \leq \lambda \text{ \& \; } |E^2 - 2| > 2, \\ (0, \gamma_{K,2}), & |E+t| > \lambda \text{ \& \; } |E^2 - 2| \leq 2, \\ (0, 0), & |E+t| \leq \lambda \text{ \& \; } |E^2 - 2| \leq 2, \end{cases} \quad (5)$$

where $\gamma_{R,1} = \max \left\{ \ln \left| \frac{\lambda c_1}{2c_2} \right|, 0 \right\}$, $\gamma_{R,2} = \ln \left| \frac{c_1}{2} \right|$, $\gamma_{K,1} = \max \left\{ \ln \left| \frac{2c_2}{\lambda c_1} \right|, 0 \right\}$ and $\gamma_{K,2} = \ln \left| \frac{c_1}{\lambda} \right|$ with $c_1 = |E^2 - 2| + \sqrt{(E^2 - 2)^2 - 4}$ and $c_2 = |E+t| + \sqrt{(E+t)^2 - \lambda^2}$ [56].

Phase diagram determined by the analytical LEs.—The MMEs and the emergent quantum phases listed in Table I, and the phase boundaries represented by dashed lines in Fig. 2, can be derived from the analytical expressions presented in Eq. (5). Mathematically, the inequality involving the absolute value yields two critical points. Consequently, each line in Eq. (5) results in four critical points ($E_c = -2, -t - \lambda, -t + \lambda, 2$), which partition the energy axis into five distinct regions.

A specific value of λ results in three distinct relationships concerning the relative positions of the four critical points: $-2 \leq -t - \lambda < -t + \lambda < 2$, $-t - \lambda < -2 < -t + \lambda < 2$, and $-t - \lambda < -2 < 2 \leq -t + \lambda$. Therefore, the discussion of the LEs must be divided into three cases: ① $\lambda \leq 2 - t$, ② $2 - t < \lambda < 2 + t$, and ③ $\lambda \geq 2 + t$.

We can further derive the values of the LEs using the inequalities in Eq. (5). Case ①: In the regions where $E < -2$ or $E > 2$, we obtain the pairs $(\gamma_R, \gamma_K) = (\gamma_{R,1}, \gamma_{K,1})$ from the inequalities $|E+t| > \lambda$ and $|E^2 - 2| > 2$ presented in the first line of Eq. (5). Consequently,

only extended states ($\gamma_R = 0$ and $\gamma_K > 0$) or localized states ($\gamma_R > 0$ and $\gamma_K = 0$) can exist within this energy interval. We can further derive two traditional MEs by setting $\gamma_{R,1} = 0$: $E_c = \pm \frac{1}{\lambda} \pm \sqrt{\frac{1}{\lambda^2} \pm \frac{2t}{\lambda}} + 2$. Moreover, the fourth line of Eq. (5) indicates that $(\gamma_R, \gamma_K) = (0, 0)$ in the region $-t - \lambda \leq E \leq -t + \lambda$, suggesting the emergence of multifractal states. Two corresponding MMEs can be identified: $E_c = \pm \lambda - t$. The remaining energy intervals can be analyzed similarly using the second and third lines of Eq. (5), leading to the conclusion that all eigenstates are extended. Thus, two-state (Extended + Multifractal) and three-state (Extended + Multifractal + Localized) coexisting quantum phases emerge under these conditions. Case ②: A similar examination can be conducted on expression (5). The results indicate that while the ME $E_c = \frac{1}{\lambda} + \sqrt{\frac{1}{\lambda^2} + \frac{2t}{\lambda}} + 2$ and the MME $E_c = \lambda - t$ remain unchanged, the ME $E_c = -\frac{1}{\lambda} - \sqrt{\frac{1}{\lambda^2} - \frac{2t}{\lambda}} + 2$ and the MME $E = -\lambda - t$ merge into one point: $E_c = -2$. Thus, only a three-state coexisting quantum phase emerges under these circumstances. Case ③: In this case, only two MMEs ($E_c = \pm 2$) are possible, leading to a two-state (Localized + Multifractal) coexisting quantum phase. This occurs because the ME $E_c = \frac{1}{\lambda} + \sqrt{\frac{1}{\lambda^2} + \frac{2t}{\lambda}} + 2$ and the MME $E_c = \lambda - t$ converge at $E_c = 2$.

Phases characterized with IPR.—We now analyze the IPR $\xi_{R(K)}$ of the eigenstates in lattice (or dual) spaces

$$\xi_{R(K)} = \sum_{n(k)=1}^N \sum_{s=a,b,c} |\psi_{n(k),s}|^4, \quad (6)$$

where $\psi_{n(k),s}$ denote the wave functions on sublattice $s = \{A, B, C\}$ within the n (k)-th primitive cell. The IPRs measure the spatial concentration of quantum states: a finite IPR (system-size-independent) signals localized states with wavefunctions peaked at few sites, while vanishing IPR ($\sim 1/N$) indicates extended states. The combined analysis of real-space and dual-space IPRs provides a practical method to distinguish multifractal, localized, and extended eigenstates. (see Table II). As the quasiperiodic intensity λ increases, a region exhibiting multifractal characteristics emerges from the flat band at $E = -t$. This observation supports the notion that multifractal states can arise from the flat band, ultimately leading to MMEs (see Fig. 2). It is noteworthy that the emergence of this multifractal region occurs exclusively when quasiperiodic modulation is applied to sublattices B or C , both of which are associated with the flat band. Furthermore, similar MMEs can also manifest in diamond flat-band lattices, as well as in cross-stitch and Lieb flat-band lattices, when subjected to partial quasiperiodic modulation [56].

Experimental realization on Rydberg atomic array.—The lattice model in Eq. (1) can be realized in various

artificial quantum systems, for specificity, we consider a Rydberg atomic array [53–55, 58–60] to illustrate the experimental scheme. The Hamiltonian for the atomic array with N unit cells in Fig. 1(c) can be expressed as

$$\begin{aligned} H_R = & \sum_n (J_{AB} \sigma_{n,A}^+ \sigma_{n,B}^- + J_{AC} \sigma_{n,A}^+ \sigma_{n,C}^- + J_{BC} \sigma_{n,B}^+ \sigma_{n,C}^- \\ & + J_{AB} \sigma_{n,B}^+ \sigma_{n+1,A}^- + J_{AC} \sigma_{n,C}^+ \sigma_{n+1,A}^- + \text{H.c.}) \\ & + \frac{1}{2} \sum_n V_n (1 + \sigma_{n,C}^z), \end{aligned} \quad (7)$$

where $\sigma^\pm = \frac{1}{2}(\sigma_x \pm i\sigma_y)$. The dipole-dipole interaction between Rydberg atoms is given by $J_{ij} = \frac{d^2}{R_{ij}^3} (3 \cos^2 \theta_{ij} - 1)$, where d represents the transition dipole moment between the two Rydberg levels, R_{ij} (with $i, j = A, B, C$) is the distance between sites i and j , and θ_{ij} is the angle between R_{ij} and the quantization axis defined by the magnetic field \mathbf{B} [58–60]. J_{ii} can be effectively mitigated to zero by selecting the magic angle $\theta_{ii} = \theta_m = 54.7^\circ$. In SM [56], we demonstrate that the model in Eq. (7) is equivalent to the model presented in Eq. (1) under the conditions that $J_{AB} = J_{AC} = J$ and $J_{BC} = t$. To achieve identical coupling J_{ij} between sublattice A and sublattices B and C , the following conditions must hold: $R_1 = \frac{2R_y}{\sin \theta_A}$, $R_2 = \sqrt{R_1^2 + R_x^2 - 2R_1 R_x \cos \theta_A}$, $R_3 = \sqrt{2R_1 R_2 \cos(\theta_1 + \theta_2)}$, where the angles $\theta_1 = \pi - \theta_m - \theta_A$, $\theta_2 = \theta_m - \arcsin\left(\frac{R_1}{R_2} \sin \theta_A\right)$, and $\theta_3 = \theta_m - \arcsin\left(\frac{2R_1}{R_3} \sin \theta_A\right)$. From these conditions, we can derive the coupling constants: $J = \frac{d^2}{R_1^3} (3 \cos^2 \theta_1 - 1) = \frac{d^2}{R_2^3} (3 \cos^2 \theta_2 - 1)$, and $t = \frac{d^2}{R_3^3} (3 \cos^2 \theta_3 - 1)$.

The LEs and IPRs can be determined through the measurement of a quantity, denoted as $P_{\beta,m}^{R/K}$, which is defined subsequently. We follow the method outlined in Ref [61] to obtain $P_{\beta,m}^R$. The dynamics of the system governed by the Hamiltonian H_R satisfy the Schrödinger equation: $|\psi(t)\rangle = e^{-iH_R t} |\psi(0)\rangle = \sum_\beta C_\beta e^{-iE_\beta t} |\psi_\beta\rangle$, where $C_\beta = \langle \psi_\beta | \psi(0) \rangle$ and $\beta \in \{1, 2, 3, \dots, 3N\}$ corresponds to the eigenvalue index. The initial state is selected as $|\psi(0)\rangle_m = |0\rangle_1 \cdots |0\rangle_{m-1} \left(\frac{|0\rangle_m + |1\rangle_m}{\sqrt{2}} \right) |0\rangle_{m+1} \cdots |0\rangle_{3N}$. During the evolution process, one can measure the time evolution curve of $\langle \sigma_m^+ \rangle = \langle \sigma_m^x \rangle + i \langle \sigma_m^y \rangle$, and subsequently apply a Fourier transform to obtain the squared modulus of the transformation for various frequencies β , denoted as $P_{\beta,m}^R$, which represents the real space distribution in site m for eigenvalue E_β [56, 61]. We can further do a Fourier transform to the real space distribution $P_{\beta,m}^R$ to obtain the corresponding distribution $P_{\beta,m}^K$ in the dual space. Upon the derivation of $P_{\beta,m}^{R/K}$, the corresponding

IPR $\xi_{R/K}$ can be directly derived using the equation:

$$\xi_{R/K}(E_\beta) = \sum_m (P_{\beta,m}^{R/K})^2. \quad (8)$$

Furthermore, the wave function of a localized state can be expressed as

$$\psi_{R/K} \propto \max\{P_{\beta,m}^{R/K}\} e^{-\gamma_{R/K}(m-m_0)}, \quad (9)$$

where $\max\{P_{\beta,m}^{R/K}\}$ represents the maximum amplitude at a fixed β , and m_0 corresponds to the site with the maximum amplitude.

We have calculated the IPRs and LEs for systems with unit cell numbers selected based on Fibonacci sequences, specifically for system sizes $N = 13, 21, 34, 55$ [56]. Figure 3 shows the experimentally measurable real-space and dual-space IPRs. Based on the analytical thresholds in Table I, we construct the phase diagram for $\lambda = 1.5$, revealing three distinct regimes: (i) localized states ($E < -2$ or $E > 2.61$), (ii) multifractal states ($-2 < E < 0.5$), and (iii) extended states ($0.5 < E < 2.61$). Remarkably, the experimentally measurable IPRs in Fig. 3 closely align with the criteria from Table II, enabling unambiguous phase discrimination. The key signatures are as follows: Localized/extended states: Real-space ξ_R and dual-space ξ_K IPRs exhibit spatial separation, with $\xi_R > \xi_K$ for localized states or $\xi_R < \xi_K$ for extended states. Multifractal states: ξ_R and ξ_K hybridize since $\xi_R \sim \xi_K$. Notably, the results in Fig. 3 demonstrate that 13-unit-cell systems suffice to capture the essential physics predicted by our model. This confirms that all three quantum phases (localized, extended, and multifractal states) are experimentally accessible with current Rydberg array platforms.

Conclusion.—We have introduced a class of one-dimensional, exactly solvable lattice models that exhibit a complete set of MMEs and multiple-state coexisting quantum phases. Moreover, these models can be readily realized in artificial quantum systems, such as Rydberg atomic arrays and superconducting circuits. Our results demonstrate that real and dual space IPRs, which are experimentally accessible, provide a criterion to unambiguously differentiate between these quantum phases.

Acknowledgements.—We thank Chang Li and Yan-Xiong Du for their insightful suggestions, Ling-Feng Yu and Rui-Jie Chen for their programming and computing support. This work was supported by the National Key Research and Development Program of China (Grant No.2022YFA1405300), Innovation Program for Quantum Science and Technology (Grant No. 2021ZD0301700), the Guangdong Basic and Applied Basic Research Foundation (Grant No.2021A1515012350), Guangdong Provincial Quantum Science Strategic Initiative(Grants No. GDZX2304002 and GDZX2404001), and the Open Fund of Key Laboratory of Atomic and

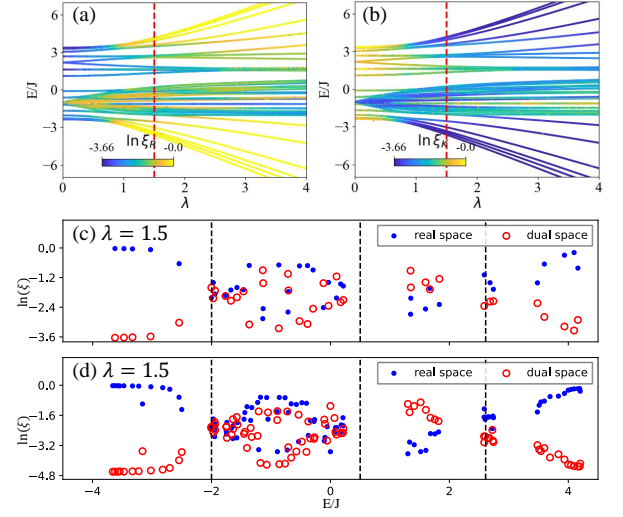


FIG. 3. The expected experimental IPRs. (a,b) The real and dual space IPRs $\xi_{R/K}$ as functions of potential strength λ and energy E/J for $N = 13$. Double space IPRs at $\lambda = 1.5$ vs E/J for (c) $N=13$ and (d) $N=34$.

Subatomic Structure and Quantum Control (Ministry of Education).

* Corresponding author: slzhu@scnu.edu.cn

† Corresponding author: lizphys@m.scnu.edu.cn

- [1] P. W. Anderson, Absence of diffusion in certain random lattices, Phys. Rev. **109**, 1492 (1958).
- [2] S. Aubry and G. André, Analyticity breaking and Anderson localization in incommensurate lattices, Ann. Israel Phys. Soc **3**, 18 (1980).
- [3] N. F. Mott, Electrons in disordered structures, Adv. Phys. **50**, 865 (1967).
- [4] F. Liu, S. Ghosh, and Y. D. Chong, Localization and adiabatic pumping in a generalized Aubry-André-Harper model, Phys. Rev. B **91**, 014108 (2015).
- [5] J. Wang, X.-J. Liu, X. Gao, and H. Hu, Phase diagram of a non-Abelian Aubry-André-Harper model with p-wave superfluidity, Phys. Rev. B **93**, 104504 (2016).
- [6] T. Geisel, R. Ketzmerick, and G. Petschel, New Class of Level Statistics in Quantum Systems with Unbounded Diffusion, Phys. Rev. Lett. **66**, 1651 (1991).
- [7] S. Y. Jitomirskaya, Metal-insulator transition for the almost Mathieu operator, Ann. Math. **150**, 1159 (1999).
- [8] T. C. Halsey, M. H. Jensen, L. P. Kadanoff, I. Procaccia, and B. I. Shraiman, Fractal measures and their singularities: The characterization of strange sets, Phys. Rev. A **33**, 1141 (1986).
- [9] A. D. Mirlin, Y. V. Fyodorov, A. Mildenberger, and F. Evers, Exact Relations between Multifractal Exponents at the Anderson Transition, Phys. Rev. Lett. **97**, 046803 (2006).
- [10] H. Hiramoto and S. Abe, Dynamics of an electron in quasiperiodic systems. II. Harper's model, J. Phys. Soc. Jpn. **57**, 1365 (1988).
- [11] R. Ketzmerick, K. Kruse, S. Kraut, and T. Geisel, What

- Determines the Spreading of a Wave Packet? Phys. Rev. Lett. **79**, 1959 (1997).
- [12] J. Mayoh and A.M. García-García, Global critical temperature in disordered superconductors with weak multifractality, Phys. Rev. B **92**, 174526 (2015).
 - [13] M.V. Feigel'man, L. B. Ioffe, V. E. Kravtsov, and E. A. Yuzbashyan, Eigenfunction Fractality and Pseudogap State near the Superconductor-Insulator Transition, Phys. Rev. Lett. **98**, 027001 (2007).
 - [14] M.V. Feigel'man, L. B. Ioffe, V. E. Kravtsov, and E. Cuevas, Fractal superconductivity near localization threshold, Ann. Phys(NY). **325**, 1390 (2010).
 - [15] Z. Fan, G.-W. Chern and S.-Z. Lin, Enhanced superconductivity in quasiperiodic crystals, Phys. Rev. Res. **3**, 023195 (2021).
 - [16] X. Zhang and M. S. Foster, Enhanced amplitude for superconductivity due to spectrum-wide wave function criticality in quasiperiodic and power-law random hopping-models, Phys. Rev.B **106**, L180503 (2022).
 - [17] X. Deng, S. Ray, S. Sinha, G. V. Shlyapnikov, and L. Santos, One-Dimensional Quasicrystals with Power-Law Hopping, Phys. Rev. Lett. **123**, 025301 (2019).
 - [18] Y. Wang, L. Zhang, W. Sun, T.-F. J. Poon, and X.-J. Liu, Quantum phase with coexisting localized, extended, and critical zones, Phys. Rev. B **106**, L140203 (2022).
 - [19] Y. Wang, Mobility edges and critical regions in a periodically kicked incommensurate optical Raman lattice, Phys. Rev. A **106**, 053312 (2022).
 - [20] X. Lin, X. Chen, G.-C. Guo, and M. Gong, General approach to the critical phase with coupled quasiperiodic chains, Phys. Rev. B **108**, 174206 (2023).
 - [21] S.-Z. Li and Z. Li, Emergent recurrent extension phase transition in a quasiperiodic chain, arXiv:2304.11811.
 - [22] R. Qi, J. Cao, and X.-P. Jiang, Multiple localization transitions and novel quantum phases induced by a staggered on-site potential, Phys. Rev. B **107**, 224201 (2023).
 - [23] Q. Dai, Z. Lu, and Z. Xu, Emergence of multifractality through cascadelike transitions in a mosaic interpolating Aubry-André-Fibonacci chain, Phys. Rev. B **108**, 144207 (2023).
 - [24] C. Guo, Multiple intermediate phases in the interpolating Aubry-André-Fibonacci model, Phys. Rev. B **109**, 174203 (2024).
 - [25] T. Liu, X. Xia, S. Longhi, and L. Sanchez-Palencia, Anomalous mobility edges in one-dimensional quasiperiodic models, SciPost Phys. **12**, 27 (2022).
 - [26] Y.-C. Zhang and Y.-Y. Zhang, Lyapunov exponent, mobility edges, and critical region in the generalized Aubry-André model with an unbounded quasiperiodic potential, Phys. Rev. B **105**, 174206 (2022).
 - [27] Z. Wang, Y. Zhang, L. Wang, and S. Chen, Engineering mobility in quasiperiodic lattices with exact mobility edges, Phys. Rev. B **108**, 174202 (2023).
 - [28] T. Liu, and X. Xu, Predicted Critical State Based on Invariance of the Lyapunov Exponent in Dual Spaces, Chin. Phys. Lett. **41** 017102 (2024).
 - [29] X.-C. Zhou, Y. Wang, T.-F. J. Poon, Q. Zhou, and X.-L. Liu, Exact new mobility edges between critical and localized states, Phys. Rev. Lett. **131**, 176401 (2023).
 - [30] B. Simon and T. Spencer, Trace class perturbations and the absence of absolutely continuous spectra, Commun. Math. Phys. **125**, 113 (1989).
 - [31] M. Gonçalves, B. Amorim, E. Castro, and P. Ribeiro, Critical Phase Dualities in 1D Exactly Solvable Quasiperiodic Models, Phys. Rev. Lett. **131**, 186303 (2023).
 - [32] M. Gonçalves, B. Amorim, E. V. Castro, and P. Ribeiro, Renormalization-group theory of 1D quasiperiodic lattice models with commensurate approximants, Phys. Rev. B **108**, L100201 (2023);
 - [33] L.-Z. Tang, S.-N. Liu, G.-Q. Zhang, and D.-W. Zhang, Topological Anderson insulators with different bulk states in quasiperiodic chains, Phys. Rev. A **105**, 063327 (2022).
 - [34] Y. Wang, X. Xu, L. Zhang, H. Yao, S. Chen, J. You, Q. Zhou, and X.-J. Liu, One-Dimensional Quasiperiodic Mosaic Lattice with Exact Mobility Edges, Phys. Rev. Lett. **125**, 196604 (2020).
 - [35] Y. Liu, Y. Wang, X.-J. Liu, Q. Zhou, and S. Chen, Exact mobility edges, \mathcal{PT} -symmetry breaking, and skin effect in one-dimensional non-Hermitian quasicrystals, Phys. Rev. B **103**, 014203 (2021).
 - [36] Y. Liu, Q. Zhou, and S. Chen, Localization transition, spectrum structure and winding numbers for one-dimensional non-Hermitian quasicrystals, Phys. Rev. B **104**, 024201 (2021).
 - [37] Y. Wang, X. Xia, J. You, Z. Zheng, and Q. Zhou, Exact mobility edges for 1D quasiperiodic models, Commun. Math. Phys. **401**, 2521 (2023).
 - [38] F. Evers and A. D. Mirlin, Anderson transitions, Rev. Mod. Phys. **80**, 1355 (2008).
 - [39] J. Biddle and S. Das Sarma, Predicted Mobility Edges in One-Dimensional Incommensurate Optical Lattices: An Exactly Solvable Model of Anderson Localization, Phys. Rev. Lett. **104**, 070601 (2010).
 - [40] J. Biddle, D. J. Priour, B. Wang, and S. Das Sarma, Localization in one-dimensional lattices with non-nearest-neighbor hopping: Generalized Anderson and Aubry-André models, Phys. Rev. B **83**, 075105 (2011).
 - [41] D.-W. Zhang, L.-Z. Tang, L.-J. Lang, H. Yan, and S.-L. Zhu, Non-hermitian topological anderson insulators, Sci. China Phys. Mech. **63**, 267062 (2020).
 - [42] H. Jiang, L.-J. Lang, C. Yang, S.-L. Zhu, and S. Chen, Interplay of non-Hermitian skin effects and Anderson localization in non-reciprocal quasiperiodic lattices, Phys. Rev. B **100**, 054301 (2019).
 - [43] S.-Z. Li, X.-J. Yu, S.-L. Zhu, and Z. Li, Anderson localization and swing mobility edge in curved spacetime, Phys. Rev. B **108**, 094209 (2023).
 - [44] S.-Z. Li, E. Cheng, S.-L. Zhu and Z. Li, Asymmetric transfer matrix analysis of Lyapunov exponents in one-dimensional non-reciprocal quasicrystals, Phys. Rev. B **110**, 134203 (2024).
 - [45] L. Wang, Z. Wang, S. Chen, Non-Hermitian butterfly spectra in a family of quasiperiodic lattices, Phys. Rev. B **110**, L060201 (2024).
 - [46] L. Wang, J. Liu, Z. Wang, and S. Chen, Exact complex mobility edges and flagellate spectra for non-Hermitian quasicrystals with exponential hoppings, Phys. Rev. B **110**, 144205 (2024).
 - [47] X. Cai, Boundary-dependent self-dualities, winding numbers, and asymmetrical localization in non-Hermitian aperiodic one-dimensional models, Phys. Rev. B **103**, 014201 (2021).
 - [48] X. Cai, Localization transitions and winding numbers for non-Hermitian Aubry-André-Harper models with off-diagonal modulations, Phys. Rev. B **106**, 214207 (2022).
 - [49] S. Ganesan, J. H. Pixley, and S. D. Sarma, Nearest

- Neighbor Tight Binding Models with an Exact Mobility Edge in One Dimension, *Phys. Rev. Lett.* **114**, 146601 (2015).
- [50] S. Roy, T. Mishra, B. Tanatar, and S. Basu, Reentrant Localization Transition in a Quasiperiodic Chain, *Phys. Rev. Lett.* **126**, 106803 (2021).
- [51] H. Yao, H. Khouldi, L. Bresque, and L. Sanchez-Palencia, Critical behavior and fractality in shallow one-dimensional quasi-periodic potentials, *Phys. Rev. Lett.* **123**, 070405 (2019),
- [52] A. Avila, Global theory of one-frequency Schrödinger operators, *Acta. Math.* **1**, 215 (2015).
- [53] S. Ebadi, T. T. Wang, H. Levine, A. Keesling, G. Semeghini, A. Omran, D. Bluvstein, R. Samajdar, H. Pichler, W. W. Ho, S. Choi, S. Sachdev, M. Greiner, V. Vuletić, and M. D. Lukin, Quantum phases of matter on a 256-atom programmable quantum simulator, *Nature (London)* **595**, 227 (2021).
- [54] C. Chen, G. Bornet, M. Bintz et al., Continuous symmetry breaking in a two-dimensional Rydberg array. *Nature* **616**, 691 (2023).
- [55] A. L. Shaw, Z. Chen, J. Choi et al. Benchmarking highly entangled states on a 60-atom analogue quantum simulator. *Nature* **628**, 71 (2024).
- [56] See Supplemental Material for details regarding the case of quasiperiodic modulation (I) and the associated Lyapunov exponents (II). Section (III) outlines the transition from analytical expressions to the phase diagram. Section (IV) presents the relevant critical exponents, while section (V) offers additional evidence supporting the universality of the theory. Section (VI) describes the experimental scheme. Section (VII) shows the measurement scheme. Section (VIII) discusses the scaling behavior of IPR. The SM includes Ref. [26, 28, 38, 52, 57, 58, 61–63].
- [57] C. Danieli, J. D. Bodyfelt, and S. Flach, Flat-band engineering of mobility edges, *Phys. Rev. B* **91**, 235134 (2015).
- [58] S. de Léséleuc, V. Lienhard, P. Scholl, D. Barredo, S. Weber, N. Lang, H. P. Büchler, T. Lahaye, and A. Browaeys, Observation of a symmetry-protected topological phase of interacting bosons with Rydberg atoms, *Science* **365**, 775 (2019).
- [59] V. Lienhard, P. Scholl, S. Weber, D. Barredo, S. de Léséleuc, R. Bai, N. Lang, M. Fleischhauer, H. P. Büchler, T. Lahaye, and A. Browaeys, Realization of a density-dependent peierls phase in a synthetic, spin-orbit coupled Rydberg system, *Phys. Rev. X* **10**, 021031 (2020).
- [60] A. Browaeys and T. Lahaye, Many-body physics with individually controlled Rydberg atoms, *Nat. Phys.* **16**, 132 (2020).
- [61] P. Roushan, C. Neill, J. Tangpanitanon, V. M. Bastidas, A. Megrant, R. Barends, Y. Chen, Z. Chen, B. Chiaro, A. Dunsworth, A. Fowler, B. Foxen, M. Giustina, E. Jeffrey, J. Kelly, E. Lucero, J. Mutus, M. Neeley, C. Quintana, D. Sank, A. Vainsencher, J. Wenner, T. White, H. Neven, D. G. Angelakis, J. Martinis, Spectroscopic signatures of localization with interacting photons in superconducting qubits, *Science* **358**, 1175 (2017).
- [62] E. H. Lieb, Two Theorems on the Hubbard Model, *Phys. Rev. Lett.* **62**, 1201 (1989).
- [63] S. Longhi, Metal-insulator phase transition in a non-Hermitian Aubry-André-Harper model, *Phys. Rev. B* **100**, 125157 (2019).

Supplementary materials for: Multifractal-enriched mobility edges and emergent quantum phases in Rydberg atomic arrays

CONTENTS

References	5
I. Quasiperiodic modulation on the "flat band irrelative" sublattice	8
II. Derivation of Lyapunov exponents	9
II-1. Real space	10
II-2. Dual space	11
III. From analytical expressions to phase diagram	12
III-1. The case of $t < 2$	13
III-2. The case of $t \geq 2$	14
IV. The corresponding critical exponents	15
V. More evidence to support the universality of the theory	16
V-1. Quasiperiodic cross-stitch lattice	16
A. The LE of lattice space	16
B. The LE of dual space	18
C. Mobility edge	19
V-2. Quasiperiodic Lieb lattice	20
A. The LE of lattice space	21
B. The LE of dual space	22
C. Mobility edge	23
VI. Experimental scheme of the Rydberg atomic array	24
VII. The measurement scheme	25
VII-1. Basic principles	25
VII-2. The comparasion of IPRs obtained by the diagonalization and spectroscopic method	28
VII-3. Scaling of IPRs in real and dual spaces	28
VII-4. The corresponding LEs	28
VII-5. Self-similarity of multifractal states	29

I. QUASIPERIODIC MODULATION ON THE "FLAT BAND IRRELATIVE" SUBLATTICE

The Hamiltonian of the diamond structure lattice with quasiperiodic potential on the sublattice A reads

$$H_R = \sum_{n=1}^N (J a_n^\dagger b_n + J a_n^\dagger c_n + t b_n^\dagger c_n + \text{H.c.}) + \sum_{n=1}^{N-1} (J b_n^\dagger a_{n+1} + J c_n^\dagger a_{n+1} + \text{H.c.}) + \sum_{n=1}^N V_{a,n} a_n^\dagger a_n, \quad (\text{S1})$$

and the corresponding eigenequations are

$$\begin{aligned} \psi_{b,n-1} + \psi_{c,n-1} + \psi_{b,n} + \psi_{c,n} + V_n \psi_{a,n} &= E \psi_{a,n}, \\ \psi_{a,n+1} + \psi_{a,n} + t \psi_{c,n} &= E \psi_{b,n}, \\ \psi_{a,n+1} + \psi_{a,n} + t \psi_{b,n} &= E \psi_{c,n}. \end{aligned} \quad (\text{S2})$$

Comparing the equations in the second and third rows, one can get $\psi_{b,n} = \psi_{c,n}$. Substituting it into the equation in the first row, we obtain recursion formula about ψ_a

$$\psi_{a,n+1} + \frac{E-t}{2}V_n\psi_{a,n} + \psi_{a,n-1} = \frac{E^2 - Et - 4}{2}\psi_{a,n}. \quad (\text{S3})$$

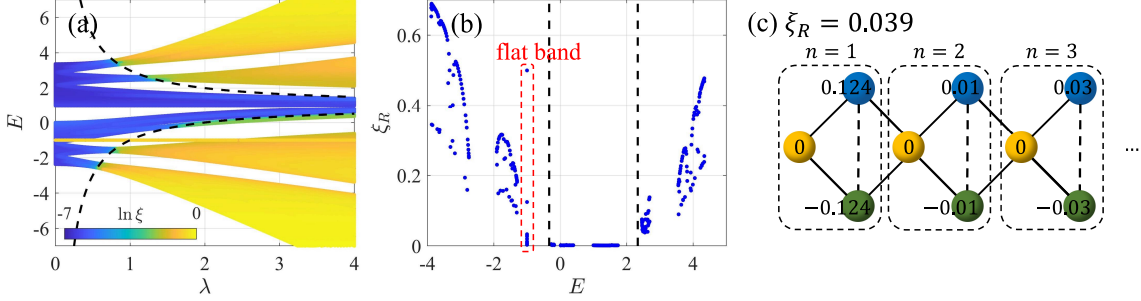


FIG. S1. (a) The IPR ξ_R versus λ , where the black dashed line is the mobility edge (ME) E_c . (b) The IPR ξ_R versus E for $\lambda = 1.5$, where the black dashed line is the ME $E_c = \pm \frac{4}{3} + 1$. (c) Amplitudes of the flat-band $E = -t$ eigenstates with IPR $\xi_R = 0.039$ in the first three unit cells at $\lambda = 1.5$. Throughout, $N = 377$ and $t = 1$.

Under the condition of $V = \frac{\lambda(E-t)}{2}$ and $E' = \frac{E^2 - Et}{2} - 2$, the result of the eigenequation is consistent with the traditional AA model, so the ME in the system can be determined by the following equation of the critical energy, i.e.,

$$\left| \frac{\lambda(E_c - t)}{2} \right| = 1. \quad (\text{S4})$$

Thus, we can obtain the MMEs' analytical expressions as

$$E_c = \pm \frac{2}{\lambda} + t. \quad (\text{S5})$$

The results given by the analytic expression as well as that by the numerical IPR are both plotted in Fig. S1(a). The results reveal that, under such circumstances, there emerges no multifractal region in the system, which means the ME E_c only separates the extended states from the localized states.

Besides, we find that the flat band at $E = -t$ is not destroyed as the quasiperiodic strength increases, which is significantly different from the case where the quasiperiodic modulation is exerted at the “flat band related” sublattice. As an example, we fix the parameter $\lambda = 1.5$, and show the corresponding IPR values of all eigenstates of the system with different E in Fig. S1(b). The results demonstrate that there are still quite a number of eigenstates in the system at the flat band $E = -t$, which is the evidence that this quasiperiodic modulation cannot destroy the flat band.

Moreover, in Fig. S1(c), we show the amplitude distribution of the wave function for a specific eigenstate ($\xi_R = 0.039$, $\lambda = 1.5$) at the flat band energy. As in the case absent of quasiperiodic modulation ($\lambda = 0$), all eigenstates corresponding to the flat band are the compact localized states [57], i.e., states with the structure of $\psi_n = (0, 1, -1)^T \delta_{n,n_0} / \sqrt{2}$, which will only appear in the B and C sublattice but not the A sublattice. This again shows that MMEs can only be induced if quasiperiodic modulation is exerted on the “flat band related” sublattice.

II. DERIVATION OF LYAPUNOV EXPONENTS

In the main text, we briefly introduce the LE in the lattice and dual spaces. Now, we exhibit a more detailed derivation process of LEs by means of Avila's global theory [52]. The definition of the LE is

$$\gamma_{R(K)} = \lim_{N \rightarrow \infty} \frac{1}{N} \ln \left\| \prod_{n(k)=1}^N T_{n(k)} \right\|, \quad (\text{S6})$$

where $\|\cdot\|$ denotes the matrix norm. $T_{n(k)}$ represents the transfer matrix and $\gamma_{R(K)}$ denotes the LE of the eigenstate for the eigenvalue E in lattice (dual) space. For localized (extended) eigenstates in lattice space, $\gamma_R > 0$ and $\gamma_K = 0$ ($\gamma_R = 0$ and $\gamma_K > 0$). For multifractal states, the wave function is delocalized in both spaces, so the LE satisfies $\gamma_R = \gamma_K = 0$ [28].

II-1. Real space

Here, we give a specific derivation of the real space LE. The Hamiltonian quantity of the real space is written as

$$H_R = \sum_{n=1}^N (Ja_n^\dagger b_n + Ja_n^\dagger c_n + tb_n^\dagger c_n + \text{H.c.}) + \sum_{n=1}^{N-1} (Jb_n^\dagger a_{n+1} + Jc_n^\dagger a_{n+1} + \text{H.c.}) + \sum_{n=1}^N V_n c_n^\dagger c_n, \quad (\text{S7})$$

and the corresponding eigenequation as

$$\psi_{c,n+1} = \frac{E^3 - (E^2 - 2)V_n - t^2 E - 4(E+t)}{2(E+t) - V_{n+1}} \psi_{c,n} - \frac{2(E+t) - V_{n-1}}{2(E+t) - V_{n+1}} \psi_{c,n-1}. \quad (\text{S8})$$

By extracting coefficients, one can obtain the corresponding transfer matrix as

$$T_n = A_n B_n, \quad (\text{S9})$$

where

$$A_n = 1/M_{n+1} \\ B_n = \begin{bmatrix} E^3 - (E^2 - 2)V_n - t^2 E - 4(E+t) & -M_{n-1} \\ M_{n+1} & 0 \end{bmatrix} \quad (\text{S10})$$

with $M_n = 2(E+t) - V_n$. According to the above expression, the LE can be divided into two parts, i.e., $\gamma_R = \gamma_A + \gamma_B$, in which [63]

$$\gamma_A = \lim_{N \rightarrow \infty} \frac{1}{N} \ln \prod_{n=1}^N \frac{1}{|2(E+t) - 2\lambda \cos(2\pi\alpha n + \theta)|} = \begin{cases} \ln \left| \frac{1}{|E+t| + \sqrt{(E+t)^2 - \lambda^2}} \right|, & |E+t| > \lambda, \\ \ln \left| \frac{1}{\lambda} \right|, & |E+t| \leq \lambda. \end{cases} \quad (\text{S11})$$

For γ_B , we apply Avila's global theory of one-frequency analytical $SL(2, \mathbb{R})$ cocycle [52]. The first step is to perform an analytical continuation of the global phase $\theta \rightarrow \theta + i\epsilon$ in B_n . In large ϵ limit, one can get

$$B_n = e^{-i2\pi\alpha n + \theta} e^\epsilon \begin{pmatrix} -\lambda E^2 - 2\lambda & \lambda e^{i2\pi\alpha} \\ -\lambda e^{-i2\pi\alpha} & 0 \end{pmatrix} + \mathcal{O}(1). \quad (\text{S12})$$

According to Avila's global theory, γ_B , as a function of ϵ , is a convex piecewise linear function with integer slopes [52]. The discontinuity of the slope occurs when E belongs to the spectrum of Hamiltonian (S7) except for $\gamma_B = 0$. Then, one can obtain

$$\gamma_B = \begin{cases} \ln \left| \lambda \frac{|E^2 - 2| + \sqrt{(E^2 - 2)^2 - 4}}{2} \right|, & |E^2 - 2| > 2, \\ \ln |\lambda|, & |E^2 - 2| \leq 2. \end{cases} \quad (\text{S13})$$

By combining γ_A (S11) and γ_B (S13), we obtain the LEs' analytical expressions with respect to the eigenvalue E in lattice space. Similarly, we can also get LEs' expressions in dual space. The complete LEs' expression in different energy region can be written as

$$\gamma_R = \begin{cases} \max \left\{ \ln \left| \frac{\lambda |E^2 - 2| + \lambda \sqrt{(E^2 - 2)^2 - 4}}{2|E+t| + 2\sqrt{(E+t)^2 - \lambda^2}} \right|, 0 \right\}, & |E+t| > \lambda \ \& \ |E^2 - 2| > 2, \\ \max \left\{ \ln \left| \frac{|E^2 - 2| + \sqrt{(E^2 - 2)^2 - 4}}{2} \right|, 0 \right\}, & |E+t| \leq \lambda \ \& \ |E^2 - 2| > 2, \\ \max \left\{ \ln \left| \frac{\lambda}{|t+E| + \sqrt{(t+E)^2 - \lambda^2}} \right|, 0 \right\}, & |E+t| > \lambda \ \& \ |E^2 - 2| \leq 2, \\ 0, & |E+t| \leq \lambda \ \& \ |E^2 - 2| \leq 2. \end{cases} \quad (\text{S14})$$

Since the logarithmic function in the second (third) row of the expression (S14) is always greater (smaller) than zero, $\gamma_R > 0$ ($\gamma_R = 0$) under the condition of $|E+t| \leq \lambda \ \& \ |E^2 - 2| > 2$ ($|E+t| > \lambda \ \& \ |E^2 - 2| \leq 2$). Then, one can

simplify the LE's expression as

$$\gamma_R = \begin{cases} \max \left\{ \ln \left| \frac{\lambda|E^2 - 2| + \lambda\sqrt{(E^2 - 2)^2 - 4}}{2|E + t| + 2\sqrt{(E + t)^2 - \lambda^2}} \right|, 0 \right\}, & |E + t| > \lambda \ \& \ |E^2 - 2| > 2, \\ \ln \left| \frac{|E^2 - 2| + \sqrt{(E^2 - 2)^2 - 4}}{2} \right|, & |E + t| \leq \lambda \ \& \ |E^2 - 2| > 2, \\ 0, & |E + t| > \lambda \ \& \ |E^2 - 2| \leq 2, \\ 0, & |E + t| \leq \lambda \ \& \ |E^2 - 2| \leq 2. \end{cases} \quad (\text{S15})$$

II-2. Dual space

The Hamiltonian in dual space reads

$$H_K = \sum_{k=1}^N (J_k a_k^\dagger b_k + J_k a_k^\dagger c_k + \text{H.c.}) + \sum_{n=1}^N (t b_n^\dagger c_n + \text{H.c.}) + \sum_{n=1}^{N-1} (\lambda c_{n+1}^\dagger c_n + \text{H.c.}). \quad (\text{S16})$$

Where $J_k = J + J e^{i(2\pi\alpha k)}$. Here, we insert a phase θ among J_k , i.e., $2\pi\alpha k \rightarrow (2\pi\alpha k + \theta)$, for the sake of the subsequent derivation of Avila's global theory. In fact, θ does not change the localization phase diagram, and in subsequent numerical calculations we set $\theta = 0$. From Hamiltonian (S16), one can obtain the corresponding eigenequation set, i.e.,

$$\begin{aligned} [1 + e^{i(2\pi\alpha k + \theta)}] \psi_{b,k} + [1 + e^{i(2\pi\alpha k + \theta)}] \psi_{c,k} &= E \psi_{a,k}, \\ [1 + e^{-i(2\pi\alpha k + \theta)}] \psi_{a,k} + t \psi_{c,k} &= E \psi_{b,k}, \\ \lambda \psi_{c,k+1} + \lambda \psi_{c,k-1} + [1 + e^{-i(2\pi\alpha k + \theta)}] \psi_{a,k} + t \psi_{b,k} &= E \psi_{c,k}. \end{aligned} \quad (\text{S17})$$

By combining the first and second rows of the above eigenequation set, we have

$$\psi_{a,k} = \frac{(t + E)[1 + e^{i(2\pi\alpha k + \theta)}]}{E^2 - 2 - 2 \cos(2\pi\alpha k + \theta)} \psi_{c,k}, \quad (\text{S18})$$

and

$$\psi_{b,k} = \frac{tE + 2 + 2 \cos(2\pi\alpha k + \theta)}{E^2 - 2 - 2 \cos(2\pi\alpha k + \theta)} \psi_{c,k}. \quad (\text{S19})$$

Then, one can obtain new eigenequations for the component ψ_c , i.e.,

$$\psi_{c,k+1} = -\frac{4t + 4E + t^2 E - E^3 - 4(t + E) \cos(2\pi\alpha k + \theta)}{\lambda[E^2 - 2 - 2 \cos(2\pi\alpha k + \theta)]} \psi_{c,k} - \psi_{c,k-1}. \quad (\text{S20})$$

Through the above equation, one can calculate the corresponding transfer matrix as

$$T_k = A_k B_k, \quad (\text{S21})$$

where

$$\begin{aligned} A_k &= \frac{1}{\lambda[E^2 - 2 - 2 \cos(2\pi\alpha k + \theta)]}, \\ B_k &= \begin{bmatrix} -4t - 4E - t^2 E + E^3 + 4(t + E) \cos(2\pi\alpha k + \theta) & -\lambda[E^2 - 2 - 2 \cos(2\pi\alpha k + \theta)] \\ \lambda[E^2 - 2 - 2 \cos(2\pi\alpha k + \theta)] & 0 \end{bmatrix}. \end{aligned} \quad (\text{S22})$$

The LE can be computed by $\gamma_K(E) = \gamma_A(E) + \gamma_B(E)$, in which [63]

$$\begin{aligned} \gamma_A &= \lim_{N \rightarrow \infty} \frac{1}{N} \ln \prod_{k=1}^N \frac{1}{\lambda[E^2 - 2 - 2 \cos(2\pi\alpha k + \theta)]} = \frac{1}{2\pi} \int_0^{2\pi} \ln \frac{1}{|\lambda[E^2 - 2 - 2 \cos(\phi)]|} d\phi \\ &= \begin{cases} \ln \left| \frac{2}{|\lambda E^2 - 2\lambda| + \sqrt{(\lambda E^2 - 2\lambda)^2 - 4\lambda^2}} \right|, & |E^2 - 2| > 2, \\ \ln \left| \frac{1}{\lambda} \right|, & |E^2 - 2| \leq 2. \end{cases} \end{aligned} \quad (\text{S23})$$

As for γ_B , one can use the Avila's global theory. The first step is to perform an analytical continuation of the global phase $\theta \rightarrow \theta + i\epsilon$ in B_k . In large ϵ limit, one can get

$$B_k = e^{-i2\pi\alpha k + \theta} e^\epsilon \begin{pmatrix} 2(t+E) & \lambda \\ -\lambda & 0 \end{pmatrix} + \mathcal{O}(1). \quad (\text{S24})$$

According to Avila's global theory, γ_B , as a function of ϵ , is a convex piecewise linear function with integer slopes [52]. One can obtain

$$\gamma_B = \begin{cases} \ln \left| 2|t+E| + 2\sqrt{(t+E)^2 - \lambda^2} \right|, & |E+t| > \lambda, \\ \ln |\lambda|, & |E+t| \leq \lambda. \end{cases} \quad (\text{S25})$$

By combining the information of γ_A and γ_B , one can obtain the corresponding LE versus E as

$$\gamma_K = \begin{cases} \max \left\{ \ln \left| \frac{2|E+t| + 2\sqrt{(E+t)^2 - \lambda^2}}{\lambda|E^2-2| + \lambda\sqrt{(E^2-2)^2 - 4}} \right|, 0 \right\}, & |E+t| > \lambda \ \& \ |E^2-2| > 2, \\ \max \left\{ \ln \left| \frac{2}{|E^2-2| + \sqrt{(E^2-2)^2 - 4}} \right|, 0 \right\}, & |E+t| \leq \lambda \ \& \ |E^2-2| > 2, \\ \max \left\{ \ln \left| \frac{|t+E| + \sqrt{(t+E)^2 - \lambda^2}}{\lambda} \right|, 0 \right\}, & |E+t| > \lambda \ \& \ |E^2-2| \leq 2, \\ 0, & |E+t| \leq \lambda \ \& \ |E^2-2| \leq 2. \end{cases} \quad (\text{S26})$$

Since the logarithmic function in the second row of the expression (S26) is always less than zero, $\gamma_K = 0$ under the condition of $|E+t| \leq \lambda \ \& \ |E^2-2| > 2$. Then, one can simplify the LE's expression as

$$\gamma_K = \begin{cases} \max \left\{ \ln \left| \frac{2|E+t| + 2\sqrt{(E+t)^2 - \lambda^2}}{\lambda|E^2-2| + \lambda\sqrt{(E^2-2)^2 - 4}} \right|, 0 \right\}, & |E+t| > \lambda \ \& \ |E^2-2| > 2, \\ 0, & |E+t| \leq \lambda \ \& \ |E^2-2| > 2, \\ \ln \left| \frac{|t+E| + \sqrt{(t+E)^2 - \lambda^2}}{\lambda} \right|, & |E+t| > \lambda \ \& \ |E^2-2| \leq 2, \\ 0, & |E+t| \leq \lambda \ \& \ |E^2-2| \leq 2. \end{cases} \quad (\text{S27})$$

The traditional ME is given by $\gamma_R = \gamma_K = 0$ for the first line of the Eq. (S15) and (S27), thus one can obtain four critical points on the energy axis, i.e.,

$$E_c = \begin{cases} \frac{1}{\lambda} + \sqrt{\frac{1}{\lambda^2} + \frac{2t}{\lambda} + 2}, \\ \frac{1}{\lambda} - \sqrt{\frac{1}{\lambda^2} + \frac{2t}{\lambda} + 2}, \\ -\frac{1}{\lambda} + \sqrt{\frac{1}{\lambda^2} - \frac{2t}{\lambda} + 2}, \\ -\frac{1}{\lambda} - \sqrt{\frac{1}{\lambda^2} - \frac{2t}{\lambda} + 2}. \end{cases} \quad (\text{S28})$$

Note that, E_c can only emerge in the energy region $|E+t| > \lambda \ \& \ |E^2-2| > 2$. Therefore, only two of the four critical points can be chosen, i.e., $E_{c,1} = \frac{1}{\lambda} + \sqrt{\frac{1}{\lambda^2} + \frac{2t}{\lambda} + 2}$ and $E_{c,2} = -\frac{1}{\lambda} - \sqrt{\frac{1}{\lambda^2} - \frac{2t}{\lambda} + 2}$. By considering the values of different parameters λ , one can directly obtain LEs in different cases.

III. FROM ANALYTICAL EXPRESSIONS TO PHASE DIAGRAM

For diamond lattice in the main text, the complete phase diagram consists of two parts, namely, the condition of $t < 2$ and $t \geq 2$. In this section, we will detail the complete process of obtaining phase diagram from analytic expression.

III-1. The case of $t < 2$

First, we discuss the case of $t < 2$. Now, we know that the LEs analytic expressions of lattice space and dual space are, respectively,

$$\gamma_R = \begin{cases} \gamma_{R,1}, & |E+t| > \lambda \ \& \ |E^2-2| > 2, \\ \gamma_{R,2}, & |E+t| \leq \lambda \ \& \ |E^2-2| > 2, \\ 0, & |E+t| > \lambda \ \& \ |E^2-2| \leq 2, \\ 0, & |E+t| \leq \lambda \ \& \ |E^2-2| \leq 2, \end{cases} \quad (\text{S29})$$

where $\gamma_{R,1} = \max \left\{ \ln \left| \lambda \frac{|E^2-2| + \sqrt{(E^2-2)^2-4}}{2|E+t| + 2\sqrt{(E+t)^2-\lambda^2}} \right|, 0 \right\}$, $\gamma_{R,2} = \ln \left| \frac{|E^2-2| + \sqrt{(E^2-2)^2-4}}{2} \right|$, and

$$\gamma_K = \begin{cases} \gamma_{K,1}, & |E+t| > \lambda \ \& \ |E^2-2| > 2, \\ 0, & |E+t| \leq \lambda \ \& \ |E^2-2| > 2, \\ \gamma_{K,2}, & |E+t| > \lambda \ \& \ |E^2-2| \leq 2, \\ 0, & |E+t| \leq \lambda \ \& \ |E^2-2| \leq 2, \end{cases} \quad (\text{S30})$$

where $\gamma_{K,1} = \max \left\{ \ln \left| \frac{2|E+t| + 2\sqrt{(E+t)^2-\lambda^2}}{\lambda|E^2-2| + \lambda\sqrt{(E^2-2)^2-4}} \right|, 0 \right\}$, $\gamma_{K,2} = \ln \left| \frac{|t+E| + \sqrt{(t+E)^2-\lambda}}{\lambda} \right|$.

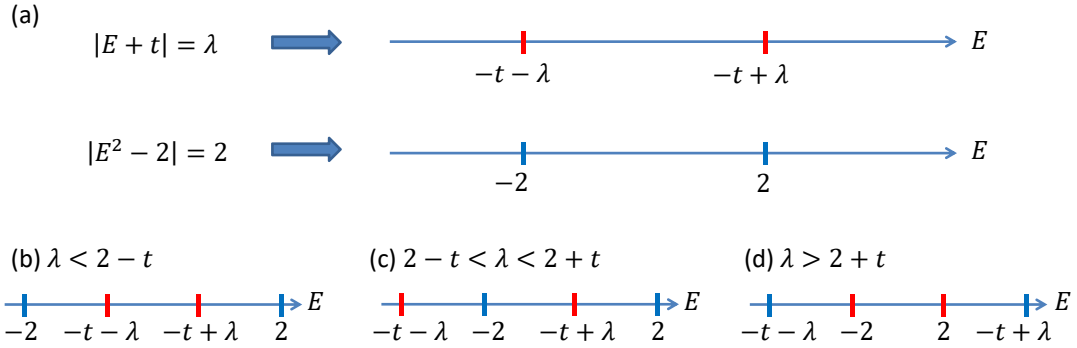


FIG. S2. (a) Four critical points on the energy axis. (b-d) Three possible relative positions of the four critical points.

From the equations (S29) and (S30), one can see that the values of LEs are determined by two inequalities no matter in the lattice space or in the dual space. Mathematically, since an inequality with an absolute value operation has two critical points, two inequalities will give four critical points [see Fig. S2]. Obviously, there are three different relationships of relative position between the four critical points, i.e.,

$$\begin{aligned} \textcircled{1} \quad & -2 < -t-\lambda < -t+\lambda < 2 \quad \text{for } \lambda \leq 2-t, \\ \textcircled{2} \quad & -t-\lambda < -2 < -t+\lambda < 2 \quad \text{for } 2-t \leq \lambda \leq 2+t, \\ \textcircled{3} \quad & -t-\lambda < -2 < 2 < -t+\lambda \quad \text{for } \lambda \geq 2+t. \end{aligned} \quad (\text{S31})$$

Furthermore, after determining the relative positions of the four critical points, one can obtain the values of LEs in different ranges on the energy axis through the information given by the inequalities. For example, let's consider case ①. We plot the process of getting the LEs' value on the energy axis in Fig. S3. As shown in the figure, we obtain that in the region of $E < -2$ or $E > 2$, the LE $\gamma_R = \gamma_{R,1}$. In other words, both $\gamma_R = \ln \left| \lambda \frac{|E^2-2| + \sqrt{(E^2-2)^2-4}}{2|E+t| + 2\sqrt{(E+t)^2-\lambda^2}} \right|$ and $\gamma_R = 0$ are valid in this region. Then, we obtain $\gamma_R \geq 0$ in the region of $E < -2$ and $E > 2$ [see Fig. S3]. Perform the same analysis on the fourth line of the expression, we obtain $\gamma = 0$ in the region of $-t-\lambda < E < -t+\lambda$.

By analyzing the inequality information given by each line of the expression (S29) and (S30) step by step, one can obtain all LEs, which includes results both in the lattice and the dual spaces. By combining the above information from the two dual spaces, one can obtain the complete set of MMEs and all possible emergent quantum phases.

under the condition of $\lambda < 2 - t$

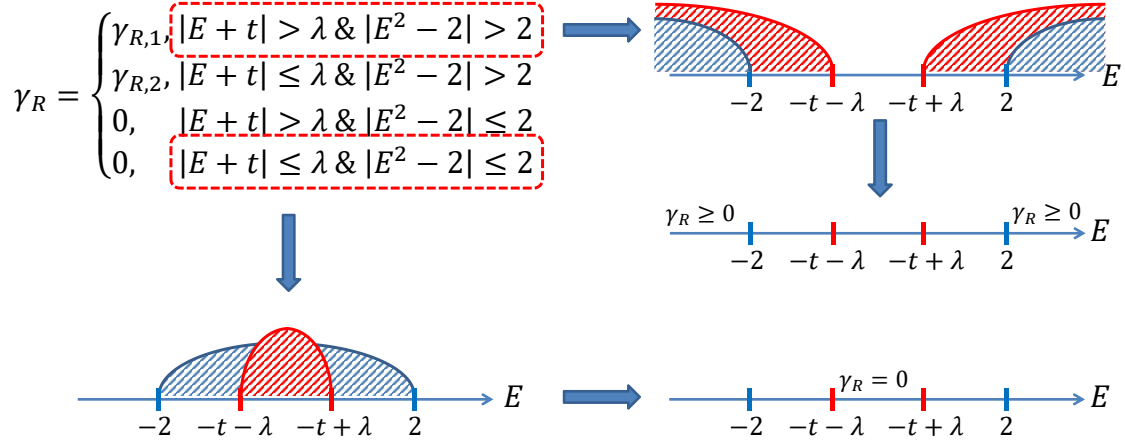


FIG. S3. The LEs for different regions determined by the analytical expressions.

III-2. The case of $t \geq 2$

Now, we turn to the case of $t \geq 2$. The main analysis process is the same as previous subsection III-1. Under such circumstances, the critical points generated by the inequality also have three relative positions on the energy axis E , i.e.,

$$\begin{aligned} \textcircled{1} \quad & t - \lambda < -t + \lambda < -2 < 2 \quad \text{for } \lambda \leq t - 2, \\ \textcircled{2} \quad & t - \lambda < -2 < -t + \lambda < 2 \quad \text{for } t - 2 \leq \lambda \leq t + 2, \\ \textcircled{3} \quad & t - \lambda < -2 < 2 < -t + \lambda \quad \text{for } \lambda \geq t + 2. \end{aligned} \quad (\text{S32})$$

The complete phase diagram can be obtained using the same analysis method as in the previous Sec. II-1. We plot the phase diagram on energy axis E for different λ in Fig. S4(a-c). The results confirm again that all types of MMEs and multi-state coexisting quantum states emerge.

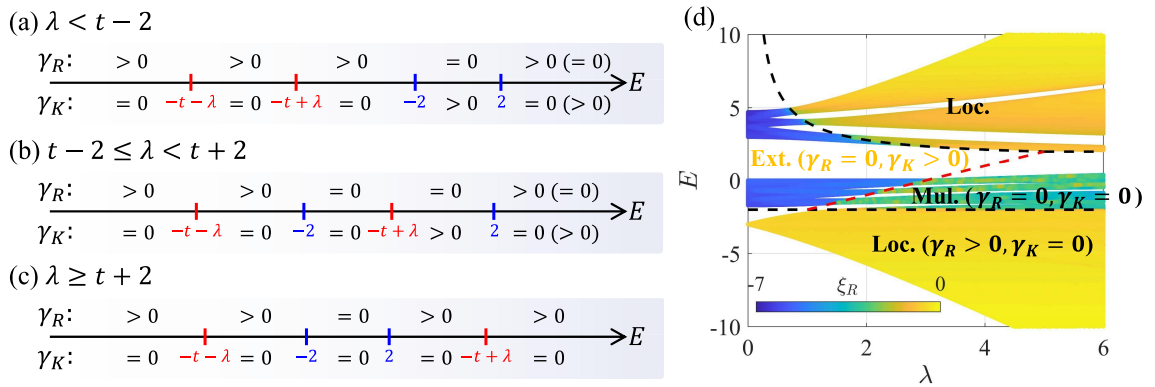


FIG. S4. LEs' Phase diagram versus E with different λ . (b) The lattice space IPR ξ_R versus λ , where the black (red) dashed line is the critical energy separating $\gamma_R > 0$ and $\gamma_R = 0$ regions ($\gamma_K > 0$ and $\gamma_K = 0$ regions) in lattice (dual) space. Throughout, $N = 377$ and $t = 1$.

Besides, the numerically calculated IPR is also shown in Fig. S4 to indicate the emergence of MMEs (in the region of $\lambda > t - 2$), which agrees perfectly with the theoretical expression (dashed lines). We summarize the results corresponding to the case of $t \geq 2$ in Tab. I.

TABLE I. MMEs and emergent quantum phases of flat-band partially-quasiperiodic diamond lattice for the case of $t \geq 2$.

Quasiperiodic strength	$\lambda < t - 2$		$t - 2 \leq \lambda < 2 + t$			$\lambda \geq t + 2$
Exact MMEs ($E_c =$)	$\frac{1}{\lambda} + \sqrt{\frac{1}{\lambda^2} + \frac{2t}{\lambda} + 2}$	-2	$\frac{1}{\lambda} + \sqrt{\frac{1}{\lambda^2} + \frac{2t}{\lambda} + 2}$	$\lambda - t$	-2	± 2
Separated states	Ext.* and Loc.	Ext. and Loc.	Ext. and Loc.	Ext. and Mul.	Ext. and Mul.	Loc. and Mul.
Possible phases	Ext.+Loc.		Ext.+Mul.+Loc.			Loc.+Mul.

*Ext.=Extended states; Loc.=Localized states; Mul.=Multifractal states.

IV. THE CORRESPONDING CRITICAL EXPONENTS

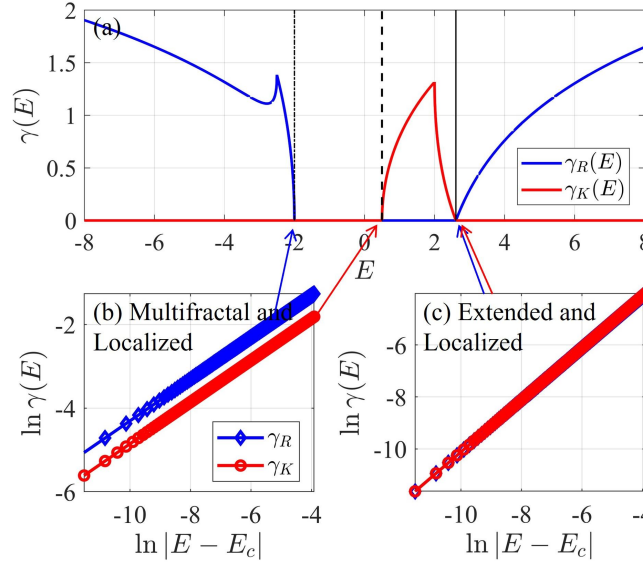


FIG. S5. (a) The LE versus E in the region of $E \in [-8, 8]$. $\ln \gamma$ versus $\ln |E - E_c|$ for the case of $E_c = -2$ and $E_c = 0.5$ (b), and the case of $E = 2.6103$ (c). The red and blue lines stand for the LEs in the lattice and dual spaces, respectively. Other parameters $t = 1$ and $\lambda = 1.5$.

Critical exponent, as an important indicator of the universal class of phase transitions, has been widely used in the study of localized phase transitions. The standard Anderson transition from the extended phase to the localized phase corresponds to a critical exponent $\mu = 1$ [38], while the corresponding critical exponent of the transition from the multifractal phase to the localized phase is 0.5 [26].

Here we calculate the critical exponent of the model in the main text and plot that in Fig. S5.

First, we exhibit the LE in lattice and dual space for all eigenenergies between $E \in [-8, 8]$ at $\lambda = 1.5$ and $t = 1$ [see Fig. S5(a)]. It can be seen clearly that the LEs for ME separating the multifractal and localized states are very different from the LE for ME separating the extended and localized states. By fitting the LEs under log-log scale, we obtain the corresponding critical exponents, which equal to the slope of $\gamma_{R(K)}$ under log-log scale in Fig. S5(b)(c). On the one hand, from Fig. S5(b), one can find that the critical exponent $\nu = 1/2$ for the critical energy separating the multifractal and localized states ($E_c = -2$ for γ_R and $E_c = 0.5$ for γ_K). On the other hand, from Fig. S5(c), the corresponding critical exponent $\nu = 1$ for the critical energy separating the extended and localized states ($E_c = 2.6103$ for both γ_R and γ_K). The critical exponent again from another perspective supports the correctness of the results given by analyzing MMEs and IPR in the main text.

V. MORE EVIDENCE TO SUPPORT THE UNIVERSALITY OF THE THEORY

In order to prove the universality of the theory, we provide another two typical flat-band partially-quasiperiodic lattice models, namely, quasiperiodic cross-stitch lattice and quasiperiodic Lieb lattice.

V-1. Quasiperiodic cross-stitch lattice

First, we discuss MMEs and the emergent multi-state coexisting quantum phase in quasiperiodic cross-stitch lattice.

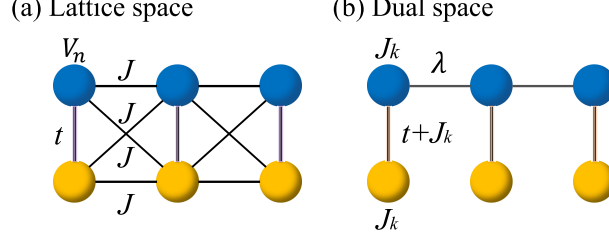


FIG. S6. The schematic diagram of the quasiperiodic cross-stitch lattice in lattice space (a) and in dual space (b). Blue and yellow balls correspond to sublattice A and B, respectively.

The geometric structure is shown schematically in Fig. S6(a) and the Hamiltonian can be written as

$$H_R = \sum_{n=1}^{N-1} J(a_n^\dagger b_{n+1} + a_n^\dagger a_{n+1} + b_n^\dagger a_{n+1} + b_n^\dagger b_{n+1} + \text{H.c.}) + \sum_{n=1}^N (ta_n^\dagger b_n + \text{H.c.}) + \sum_{n=1}^N V_n a_n^\dagger a_n, \quad (\text{S33})$$

where a_n (a_n^\dagger) and b_n (b_n^\dagger) represent the annihilation (creation) operators of sublattices A and B in the n -th unit cell, respectively. J and t denote the inter- and intra-hopping strength, which are marked in the Fig. S6. N represents the total number of unit cells. The quasiperiodic potential $V_n = 2\lambda \cos(2\pi\alpha n + \theta)$ is applied only on the sublattice A, where λ , α , and θ denote the quasiperiodic strength, an irrational number, and a phase offset, respectively. Under the condition of $\lambda = 0$, Hamiltonian (S33) will exhibit two bands with different dispersion relations. One is an exact flat-band of $E_k = -t$, while the other is a dispersive band of $E_k = 4J \cos(k) + t$ [57].

By applying dual transform $a_n = \frac{1}{\sqrt{N}} \sum_k a_k e^{-i2\pi\alpha kn}$ and $b_n = \frac{1}{\sqrt{N}} \sum_k b_k e^{-i2\pi\alpha kn}$ for Hamiltonian (S33), one can get the Hamiltonian in dual space, which has a similar structure to a Fano defect quasiperiodic lattice [see Fig. S6(b)], i.e.,

$$H_K = \sum_{k=1}^{N-1} (\lambda a_k^\dagger a_{k+1} + \text{H.c.}) + \sum_{k=1}^N [(t + J_k) a_k^\dagger b_k + \text{H.c.}] + \sum_{k=1}^N J_k (a_k^\dagger a_k + b_k^\dagger b_k), \quad (\text{S34})$$

where $J_k = 2J \cos(2\pi\alpha k + \theta)$.

A. The LE of lattice space

The eigenequation set for Hamiltonian (S33) is

$$\begin{aligned} \psi_{a,n-1} + \psi_{a,n+1} + \psi_{b,n-1} + \psi_{b,n+1} + t\psi_{b,n} &= (E - V_n)\psi_{a,n}, \\ \psi_{a,n-1} + \psi_{a,n+1} + \psi_{b,n-1} + \psi_{b,n+1} + t\psi_{a,n} &= E\psi_{b,n}. \end{aligned} \quad (\text{S35})$$

One can get the relationship between $\psi_{a,n}$ and $\psi_{b,n}$ as $\psi_{b,n} = (E + t - V_n)/(E + t)\psi_{a,n}$. Thus, from Eq. (S35), we obtain a new equation for the component $\psi_{a,n}$, i.e.,

$$\psi_{a,n+1} = \frac{E^2 - 2Et - t^2 - EV_n}{2(E + t) - V_{n+1}} \psi_{a,n} - \frac{2(E + t) - V_{n-1}}{2(E + t) - V_{n+1}} \psi_{a,n-1}, \quad (\text{S36})$$

from which we directly obtain the corresponding transfer matrix

$$T_n = A_n B_n, \quad (\text{S37})$$

where

$$A_n = \frac{1}{2(E+t) - V_{n+1}}, \quad B_n = \begin{pmatrix} E^2 - 2Et - t^2 - EV_n & -2(E+t) + V_{n-1} \\ 2(E+t) - V_{n+1} & 0 \end{pmatrix}. \quad (\text{S38})$$

The LE can be written as $\gamma_R = \gamma_A + \gamma_B$, in which

$$\begin{aligned} \gamma_A &= \lim_{N \rightarrow \infty} \frac{1}{N} \ln \prod_{n=1}^N \frac{1}{|2(E+t) - 2\lambda \cos[2\pi\alpha(n+1) + \theta]|} \\ &= \frac{1}{2\pi} \int_0^{2\pi} \ln \frac{1}{|2(E+t) + 2\lambda \cos(\phi)|} d\phi \\ &= \begin{cases} \ln \left| \frac{1}{|E+t| + \sqrt{(E+t)^2 - \lambda^2}} \right|, & |E+t| > \lambda, \\ \ln \left| \frac{1}{\lambda} \right|, & |E+t| \leq \lambda. \end{cases} \end{aligned} \quad (\text{S39})$$

As for γ_B , we apply Avila's global theory of one-frequency analytical $SL(2, \mathbb{R})$ cocycle [52]. The first step is to perform an analytical continuation of the global phase $\theta \rightarrow \theta + i\epsilon$ in B_n . In large ϵ limit, one can get

$$B_{n,\epsilon \rightarrow \infty} = e^{-i2\pi\alpha n + \theta} e^\epsilon \begin{pmatrix} -\lambda E & \lambda e^{i2\pi\alpha} \\ -\lambda e^{-i2\pi\alpha} & 0 \end{pmatrix} + \mathcal{O}(1). \quad (\text{S40})$$

According to Avila's global theory, as a function of ϵ , $\gamma_B(E)$ is a convex piecewise linear function with integer slopes [52]. The discontinuity of the slope occurs when E belongs to the spectrum of Hamiltonian H except for $\gamma_B(E) = 0$, which represents the extended states. One can get

$$\gamma_B(E) = \begin{cases} \ln \left| \frac{|\lambda E| + \sqrt{(\lambda E)^2 - 4\lambda^2}}{2} \right|, & |E| > 2, \\ \ln |\lambda|, & |E| \leq 2. \end{cases} \quad (\text{S41})$$

Combining the information of γ_A and γ_B , we obtain the LE γ_R versus E as

$$\gamma_R = \begin{cases} \max \left\{ \ln \left| \frac{|\lambda E| + \sqrt{(\lambda E)^2 - 4\lambda^2}}{2(E+t) + 2\sqrt{(E+t)^2 - \lambda^2}} \right|, 0 \right\}, & |E+t| > \lambda \text{ \& } |E| > 2, \\ \max \left\{ \ln \left| \frac{|E| + \sqrt{E^2 - 4}}{2} \right|, 0 \right\}, & |E+t| \leq \lambda \text{ \& } |E| > 2, \\ \max \left\{ \ln \left| \frac{\lambda}{|E+t| + \sqrt{(E+t)^2 - \lambda^2}} \right|, 0 \right\}, & |E+t| > \lambda \text{ \& } |E| \leq 2, \\ 0, & |E+t| \leq \lambda \text{ \& } |E| \leq 2. \end{cases} \quad (\text{S42})$$

Since the second (third) row of the LE expression satisfies $|E| > 2$ ($|E+t| < 2$), then $\gamma_R > 0$ ($\gamma_R = 0$). Finally, one can obtain the LE in the lattice space as

$$\gamma_R = \begin{cases} \max \left\{ \ln \left| \frac{|\lambda E| + \sqrt{(\lambda E)^2 - 4\lambda^2}}{2(E+t) + 2\sqrt{(E+t)^2 - \lambda^2}} \right|, 0 \right\}, & |E+t| > \lambda \text{ \& } |E| > 2, \\ \ln \left| \frac{|E| + \sqrt{E^2 - 4}}{2} \right|, & |E+t| \leq \lambda \text{ \& } |E| > 2, \\ 0, & |E+t| > \lambda \text{ \& } |E| \leq 2, \\ 0, & |E+t| \leq \lambda \text{ \& } |E| \leq 2. \end{cases} \quad (\text{S43})$$

B. The LE of dual space

The eigenequation set of dual Hamiltonian (S34) is

$$\begin{aligned}\lambda(\psi_{a,k-1} + \psi_{a,k+1}) + J_k\psi_{a,k} + (t + J_k)\psi_{b,k} &= E\psi_{a,k}, \\ (t + J_k)\psi_{a,k} + J_k\psi_{b,k} &= E\psi_{b,k}.\end{aligned}\tag{S44}$$

Then, the corresponding transfer matrix in dual space is

$$T_k = A_k B_k,\tag{S45}$$

where

$$\begin{aligned}A_k &= \frac{1}{E - 2\cos(2\pi\alpha k + \theta)}, \\ B_k &= \begin{pmatrix} \frac{E^2 - 2(2E + 2t)\cos(2\pi\alpha k + \theta) - t^2}{E - 2\cos(2\pi\alpha k + \theta)} & -E + 2\cos(2\pi\alpha k + \theta) \\ \lambda & 0 \end{pmatrix}.\end{aligned}\tag{S46}$$

The LE can be written as $\gamma_R(E) = \gamma_A(E) + \gamma_B(E)$, in which

$$\begin{aligned}\gamma_A &= \lim_{N \rightarrow \infty} \frac{1}{N} \ln \prod_{k=1}^N \frac{1}{E - 2\cos(2\pi\alpha k + \theta)} = \frac{1}{2\pi} \int_0^{2\pi} \ln \frac{1}{|E + 2\cos(\phi)|} d\phi \\ &= \begin{cases} \ln \left| \frac{1}{|E| + \sqrt{(E)^2 - 4}} \right|, & |E + t| > \lambda, \\ 0, & |E + t| \leq \lambda. \end{cases}\end{aligned}\tag{S47}$$

As for γ_B , we apply Avila's global theory of one-frequency analytical $SL(2, \mathbb{R})$ cocycle [52]. The first step is to perform an analytical continuation of the global phase $\theta \rightarrow \theta + i\epsilon$ in B_k . In large ϵ limit, one can get

$$B_{k,\epsilon \rightarrow \infty} = e^{-i2\pi\alpha k + \theta} e^\epsilon \begin{pmatrix} -(2E + 2t) & 1 \\ -1 & 0 \end{pmatrix} + \mathcal{O}(1).\tag{S48}$$

According to Avila's global theory, as a function of ϵ , $\gamma_B(E)$ is a convex piecewise linear function with integer slopes [52]. The discontinuity of the slope occurs when E belongs to the spectrum of Hamiltonian H except for $\gamma_B(E) = 0$, which represents the extended states. One can obtain

$$\gamma_B = \begin{cases} \ln \left| \frac{|E + t| + \sqrt{(E + t)^2 - \lambda^2}}{\lambda} \right|, & |E + t| > \lambda, \\ 0, & |E + t| \leq \lambda. \end{cases}\tag{S49}$$

Combining with $\gamma_A(E)$, the LE for different E is

$$\gamma_K = \begin{cases} \max \left\{ \ln \left| \frac{2(E + t) + 2\sqrt{(E + t)^2 - \lambda^2}}{\lambda(E + \sqrt{E^2 - 4})} \right|, 0 \right\}, & |E + t| > \lambda \ \& \ |E| > 2, \\ \max \left\{ \ln \left| \frac{2}{|E| + \sqrt{E^2 - 4}} \right|, 0 \right\}, & |E + t| \leq \lambda \ \& \ |E| > 2, \\ \max \left\{ \ln \left| \frac{|E + t| + \sqrt{(E + t)^2 - \lambda^2}}{\lambda} \right|, 0 \right\}, & |E + t| > \lambda \ \& \ |E| \leq 2, \\ 0, & |E + t| \leq \lambda \ \& \ |E| \leq 2. \end{cases}\tag{S50}$$

Since the second (third) row of the LE satisfies $|E| > 2$ ($|E + t| < 2$), $\gamma_K = 0$ ($\gamma_K > 0$). Finally, one can obtain the LE of the lattice space as

$$\gamma_K = \begin{cases} \max \left\{ \ln \left| \frac{2(E + t) + 2\sqrt{(E + t)^2 - \lambda^2}}{\lambda(E + \sqrt{E^2 - 4})} \right|, 0 \right\}, & |E + t| > \lambda \ \& \ |E| > 2, \\ 0, & |E + t| \leq \lambda \ \& \ |E| > 2, \\ \ln \left| \frac{|E + t| + \sqrt{(E + t)^2 - \lambda^2}}{\lambda} \right|, & |E + t| > \lambda \ \& \ |E| \leq 2, \\ 0, & |E + t| \leq \lambda \ \& \ |E| \leq 2. \end{cases}\tag{S51}$$

C. Mobility edge

By comparing the expressions of γ_R and γ_K , one can find that in the region of $|E+t| \leq \lambda$ & $|E| \leq 2$, $\gamma_R = \gamma_K = 0$, indicating that the corresponding eigenstates in this region are multifractal critical states. For the rest of the energy region, the lattice and dual spaces have opposite localization properties, i.e., $\gamma_R = 0$ while $\gamma_K > 0$, or vice versa. Since the critical points satisfy a mirror-symmetric relationship between the case of $t < 0$ and the case of $t > 0$, here we will only exhibit the case of $t > 0$ as what we have done in the main text.

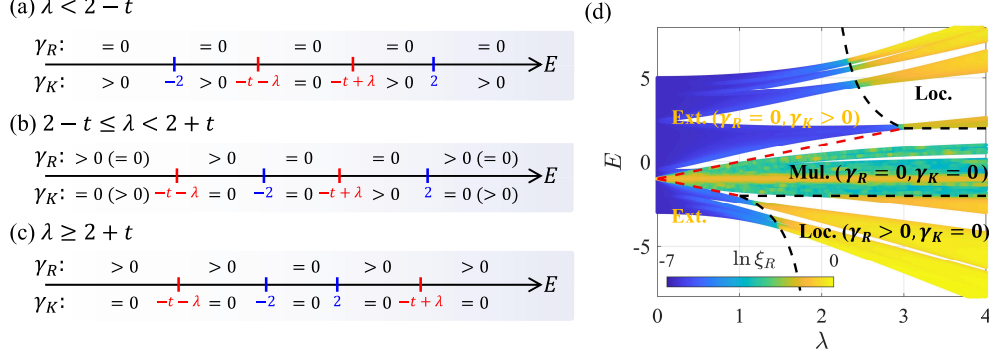


FIG. S7. (a-c) Phase diagram versus E with different λ for the case of $t < 2$. (d) The lattice space IPR ξ_R versus λ , where the black (red) dashed line is the critical energy separating $\gamma_R > 0$ and $\gamma_R = 0$ regions ($\gamma_K > 0$ and $\gamma_K = 0$ regions) in lattice (dual) space. The other parameters $N = 610$ and $t = 1$.

On the one hand, for the case of $t < 2$, from the inequalities in the analytic expressions (S43) and (S51), one can find that the cross-stitch model has the same four critical points as the diamond model in the main text, and they also divide the energy axis into five intervals. The difference lies in that $E_c = \frac{2t}{\lambda-2}$ does not fall within the energy interval $|E+t| > \lambda$ and $|E| > 2$ under the conditions of $\lambda < 2 - t$ and $\lambda \geq 2 + t$. That is to say, the three-state coexisting quantum phase can only emerge when $2 - t \leq \lambda < 2 + t$. In other words, since there is no localized (extended) state in the region of $\lambda < 2 - t$ ($\lambda \geq 2 + t$), only two-state coexisting quantum phases can emerge in certain circumstances [see Fig. S7(a-c)]. Furthermore, we numerically compute the corresponding IPR [see Fig. S7(d)]. The numerical results and analytical results show that MMEs and multi-state coexisting quantum phases will emerge in the system.

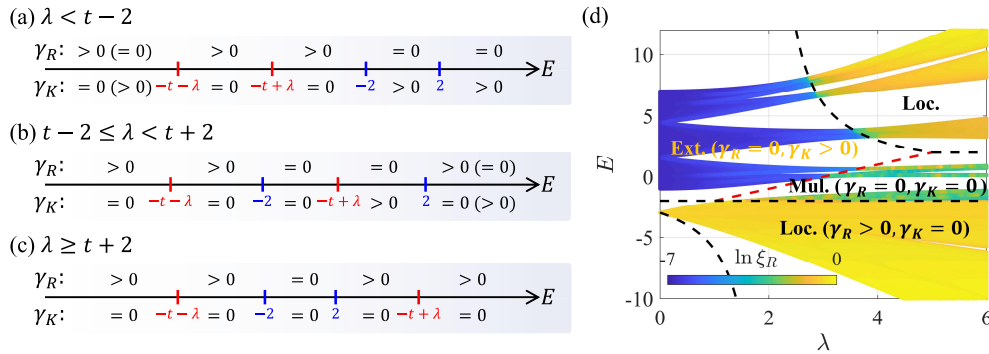


FIG. S8. (a-c) Phase diagram versus E with different λ for the case of $t \geq 2$. (d) The lattice space IPR ξ_R versus λ , where the black (red) dashed line is the critical energy separating $\gamma_R > 0$ and $\gamma_R = 0$ regions ($\gamma_K > 0$ and $\gamma_K = 0$ regions) in lattice (dual) space. The other parameters $N = 610$ and $t = 3$.

A similar analysis leads us to the phase diagram for $t \geq 2$, which is plotted in Fig. S8(a-c). The main difference between $t \leq 2$ and $t < 2$ is in the first stage of the phase diagram, i.e., the case of $\lambda < t - 2$. Under certain circumstances, the four critical points satisfy the relative position relation $-t - \lambda < -t + \lambda < -2 < 2$. By analyzing the interval given by the inequalities of the expressions (S43) and (S51), we find that it is impossible to have a region with multifractal states in this case. In other words, the system has only extended and localized states in this case. In the second stage ($2 - t < \lambda < 2 + t$), multi-state coexisting quantum phases emerge in the system and all types of MMEs are allowed [see Fig. S8(b)]. In the third stage ($\lambda \geq 2 + t$), the system has only MMEs separating the localized

state and the multifractal state [see Fig. S8(c)]. Furthermore, we provide the numerical IPR [see Fig. S8(d)], which is consistent with the conclusion given by the analytic expressions.

TABLE II. MMEs and quantum phases of partially-quasiperiodic cross-stitch lattice for the case of $t < 2$

Quasiperiodic strength	$\lambda < 2 - t$	$2 - t \leq \lambda < 2 + t$			$\lambda \geq 2 + t$
Exact MMEs ($E_c =$)	$\pm\lambda - t$	$\frac{2t}{\lambda-2}$	$\lambda - t$	-2	± 2
Separated states	Ext.* and Mul.	Ext. and Loc.	Ext. and Mul.	Loc. and Mul.	Loc. and Mul.
Possible phases	Ext.+Mul.	Ext.+Mul.+Loc.			Loc.+Mul.

*Ext.=Extended states; Loc.=Localized states; Mul.=Multifractal states.

TABLE III. MMEs and quantum phases of partially-quasiperiodic cross-stitch lattice for the case of $t \geq 2$

Quasiperiodic strength	$\lambda < t - 2$		$2 - t \leq \lambda < 2 + t$			$\lambda \geq 2 + t$
Exact MMEs ($E_c =$)	$\frac{2t}{\lambda-2}$	-2	$\frac{2t}{\lambda-2}$	$\lambda - t$	-2	± 2
Separated states	Ext.* and Loc.	Ext. and Loc.	Ext. and Loc.	Ext. and Mul.	Ext. and Mul.	Loc. and Mul.
Possible phases	Ext.+Loc.		Ext.+Mul.+Loc.			Loc.+Mul.

*Ext.=Extended states; Loc.=Localized states; Mul.=Multifractal states.

Finally, we summarize the MMEs and emergent quantum phases of the partially-quasiperiodic cross-stitch lattice in Tab. II and Tab. III. The results reveal that the system contains not only the traditional ME separating extended and localized states, but also the MMEs separating multifractal and localized states or separating multifractal and extended states. Meanwhile, exotic quantum phases featuring two-state coexistence (Ext. + Loc. or Loc. + Mul.) and three-state coexistence (Ext. + Mul. + Loc.) emerge.

This is another evidence supporting the conclusion: The MMEs and exotic quantum phases can emerge in the flat-band system.

V-2. Quasiperiodic Lieb lattice

Now, we will show another quasiperiodic flat-band model, i.e., the quasiperiodic Lieb lattice [62], and the schematic diagram is shown in Fig. S9(a). The corresponding Hamiltonian reads

$$H_R = \sum_{n=1}^N (ta_n^\dagger b_n + Jb_n^\dagger c_n + \text{H.c.}) + \sum_{n=1}^N (J'b_{n+1}^\dagger c_n + \text{H.c.}) + \sum_{n=1}^N V_n a_n^\dagger a_n, \quad (\text{S52})$$

where $V_n = 2\lambda \cos(2\pi\alpha n + \theta)$. By means of the dual transform, one can obtain the Hamiltonian in dual space as

$$H_K = \sum_{k=1}^{N-1} \lambda (a_k^\dagger a_{k+1} + \text{H.c.}) + \sum_{k=1}^N [ta_k^\dagger b_k + (J + J')b_k^\dagger c_k + \text{H.c.}], \quad (\text{S53})$$

and the schematic diagram is shown in Fig. S9(b), where $J'_k = J' e^{i(2\pi\alpha k + \theta)}$. When $\lambda = 0$, the Hamiltonian (S52) has a flat band $E = 0$. For the following discuss, we set $J = J' = t = 1$ as the unit energy.

Note that, unlike the two flat-band models discussed earlier, the relative positions of the four critical points in this model are symmetric about the origin, so there are only two possibilities, namely $[-2, 2] \subseteq [-J' - 1, J' + 1]$, or $[-J' - 1, J' + 1] \subseteq [-2, 2]$. The obtained phase diagram is shown in Fig. S9(b). The corresponding IPR has also been given in Fig. S9(c).

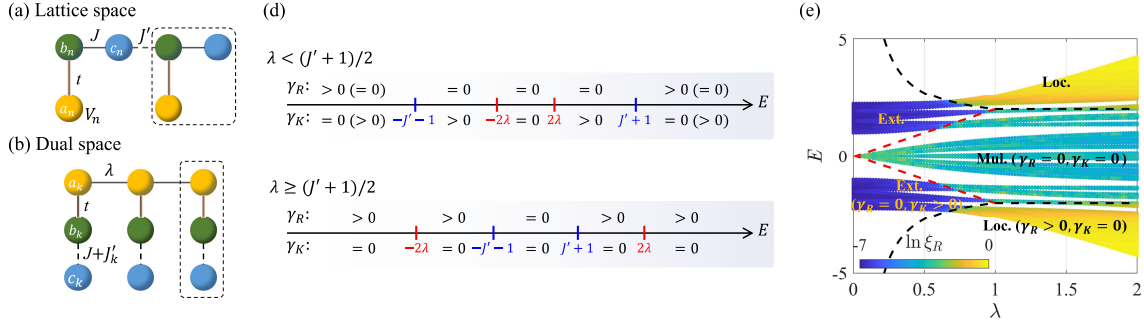


FIG. S9. (a) Lattice structure in real space and dual space. (b) The phase diagram of Lieb model. (c) IPR in lattice space ξ_R versus E for different λ , where the black (red) dashed line is the critical energy separating $\gamma_R(E) > 0$ ($\gamma_K(E) > 0$) and $\gamma_R(E) = 0$ ($\gamma_K(E) = 0$) in lattice (dual) space. In the computation, we set unit cell number $N = 377$.

A. The LE of lattice space

The eigenequation set for Hamiltonian (S52) is

$$\begin{aligned} V_n \psi_{a,n} + t \psi_{b,n} &= E \psi_{a,n}, \\ J' \psi_{c,n-1} + t \psi_{a,n} + \psi_{c,n} &= E \psi_{b,n}, \\ \psi_{b,n} + J' \psi_{b,n+1} &= E \psi_{c,n}. \end{aligned} \quad (\text{S54})$$

Then, by simplifying the Eq. (S54), one can get

$$\psi_{c,n+1} = \frac{(E^2 - J'^2 - 1)(E - V_n) - Et^2}{J'(E - V_n)} \psi_{c,n} - \psi_{c,n-1}. \quad (\text{S55})$$

Then, one can directly obtain the corresponding transfer matrix

$$T_n = A_n B_n, \quad (\text{S56})$$

where

$$\begin{aligned} A_n &= \frac{1}{J'[E - 2\lambda \cos(2\pi\alpha n + \theta)]}, \\ B_n &= \begin{pmatrix} (E^2 - J'^2 - 1)(E - V_n) - Et^2 & -J'(E - V_n) \\ J'(E - V_n) & 0 \end{pmatrix}. \end{aligned} \quad (\text{S57})$$

The LE can be written as $\gamma_R(E) = \gamma_A(E) + \gamma_B(E)$, in which

$$\begin{aligned} \gamma_A(E) &= \lim_{N \rightarrow \infty} \frac{1}{N} \ln \prod_{n=1}^N \frac{1}{J'[E - 2\lambda \cos(2\pi\alpha n + \theta)]} \\ &= \begin{cases} \ln \left| \frac{2}{J'(|E| + \sqrt{E^2 - 4\lambda^2})} \right|, & |E| > 2\lambda, \\ \ln \left| \frac{1}{J'\lambda} \right|, & |E| \leq 2\lambda. \end{cases} \end{aligned} \quad (\text{S58})$$

For $\gamma_B(E)$, again, we apply Avila's global theory of one-frequency analytical $SL(2, \mathbb{R})$ cocycle [52]. The first step in the calculation is to perform an analytical continuation of the global phase $\theta \rightarrow \theta + i\epsilon$ in B_n . In large ϵ limit, one can obtain

$$B_{n,\epsilon \rightarrow \infty} = e^{-i2\pi\alpha n + \theta} e^\epsilon \begin{pmatrix} -\lambda(E^2 - J'^2 - 1) & J'\lambda \\ -J'\lambda & 0 \end{pmatrix} + \mathcal{O}(1). \quad (\text{S59})$$

According to Avila's global theory, as a function of ϵ , $\gamma_B(E)$ is a convex piecewise linear function with integer slopes [52]. The discontinuity of the slope occurs when E belongs to the spectrum of Hamiltonian H except for

$\gamma_B(E) = 0$, which represents the extended states. Then, one can get

$$\gamma_B = \begin{cases} \ln \left| \lambda \frac{|E^2 - J'^2 - 1| + \sqrt{(E^2 - J'^2 - 1)^2 - 4J'^2}}{2} \right|, & |E^2 - J'^2 - 1| > 2J', \\ \ln |J'\lambda|, & |E^2 - J'^2 - 1| \leq 2J'. \end{cases} \quad (\text{S60})$$

Combining with γ_A , the LE for different E is

$$\gamma_R = \begin{cases} \max \left\{ \ln \left| \frac{\lambda |E^2 - J'^2 - 1| + \lambda \sqrt{(E^2 - J'^2 - 1)^2 - 4J'^2}}{J'(|E| + \sqrt{E^2 - 4\lambda^2})} \right|, 0 \right\}, & |E| > 2\lambda \ \& \ |E^2 - J'^2 - 1| > 2J', \\ \max \left\{ \ln \left| \frac{|E^2 - J'^2 - 1| + \sqrt{(E^2 - J'^2 - 1)^2 - 4J'^2}}{2J'} \right|, 0 \right\} > 0, & |E| \leq 2\lambda \ \& \ |E^2 - J'^2 - 1| > 2J', \\ \max \left\{ \ln \left| \frac{2\lambda}{|E| + \sqrt{E^2 - 4\lambda^2}} \right|, 0 \right\} = 0, & |E| > 2\lambda \ \& \ |E^2 - J'^2 - 1| \leq 2J', \\ 0, & |E| \leq 2\lambda \ \& \ |E^2 - J'^2 - 1| \leq 2J'. \end{cases} \quad (\text{S61})$$

For the energy interval in the second (third) row, since $|E^2 - J'^2 - 1| > 2J'$ ($|E| > 2\lambda$), it follows that $\gamma_R > 0$ ($\gamma_R = 0$). Therefore, the final LE of the system in real space is

$$\gamma_R = \begin{cases} \max \left\{ \ln \left| \frac{\lambda |E^2 - J'^2 - 1| + \lambda \sqrt{(E^2 - J'^2 - 1)^2 - 4J'^2}}{J'(|E| + \sqrt{E^2 - 4\lambda^2})} \right|, 0 \right\}, & |E| > 2\lambda \ \& \ |E^2 - J'^2 - 1| > 2J', \\ \ln \left| \frac{|E^2 - J'^2 - 1| + \sqrt{(E^2 - J'^2 - 1)^2 - 4J'^2}}{2J'} \right|, & |E| \leq 2\lambda \ \& \ |E^2 - J'^2 - 1| > 2J', \\ 0, & |E| > 2\lambda \ \& \ |E^2 - J'^2 - 1| \leq 2J', \\ 0, & |E| \leq 2\lambda \ \& \ |E^2 - J'^2 - 1| \leq 2J'. \end{cases} \quad (\text{S62})$$

B. The LE of dual space

The eigenequation set for dual space Hamiltonian (S53) is

$$\begin{aligned} t\psi_{b,k} + \lambda\psi_{a,k-1} + \lambda\psi_{a,k+1} &= E\psi_{a,k}, \\ t\psi_{a,k} + (J + J'e^{i(2\pi\alpha k + \theta)})\psi_{c,k} &= E\psi_{b,k}, \\ (J + J'e^{-i(2\pi\alpha k + \theta)})\psi_{b,k} &= E\psi_{c,k}. \end{aligned} \quad (\text{S63})$$

Similarly, by simplifying the eigenequation set, one can get

$$\psi_{a,n+1} = \frac{E^3 - E(2J' - 1 - t^2) - 2EJ' \cos(2\pi\alpha k + \theta)}{\lambda[E^2 - J'^2 - 1 - 2J' \cos(2\pi\alpha k + \theta)]} \psi_{a,n} - \psi_{a,n-1} \quad (\text{S64})$$

Then, one can directly obtain the corresponding transfer matrix

$$T_k = A_k B_k, \quad (\text{S65})$$

where

$$\begin{aligned} A_k &= \frac{1}{\lambda[E^2 - J'^2 - 1 - 2J' \cos(2\pi\alpha k + \theta)]}, \\ B_k &= \begin{pmatrix} E^3 - E(2J' - 1 - t^2) - 2EJ' \cos(2\pi\alpha k + \theta) & -\lambda[E^2 - J'^2 - 1 - 2J' \cos(2\pi\alpha k + \theta)] \\ \lambda[E^2 - J'^2 - 1 - 2J' \cos(2\pi\alpha k + \theta)] & 0 \end{pmatrix}. \end{aligned} \quad (\text{S66})$$

Then, LE can be written as $\gamma_R(E) = \gamma_A(E) + \gamma_B(E)$, where

$$\begin{aligned} \gamma_A &= \lim_{N \rightarrow \infty} \frac{1}{N} \ln \prod_{k=1}^N \frac{1}{\lambda[E^2 - J'^2 - 1 - 2J' \cos(2\pi\alpha k + \theta)]} \\ &= \begin{cases} \ln \left| \frac{2}{\lambda(|E^2 - J'^2 - 1| + \sqrt{(E^2 - J'^2 - 1)^2 - 4J'^2})} \right|, & |E^2 - J'^2 - 1| > 2J', \\ \ln \left| \frac{1}{J'\lambda} \right|, & |E^2 - J'^2 - 1| \leq 2J'. \end{cases} \end{aligned} \quad (\text{S67})$$

As for γ_B , by applying Avila's global theory, one can get

$$\gamma_B = \begin{cases} \ln \left| \frac{|EJ'| + J'\sqrt{(E)^2 - 4\lambda^2}}{2} \right|, & |E| > 2\lambda, \\ \ln |J'\lambda|, & |E| \leq 2\lambda. \end{cases} \quad (\text{S68})$$

Combining with γ_A , the LE for different E is

$$\gamma_K = \begin{cases} \max \left\{ \ln \left| \frac{J'(|E| + \sqrt{E^2 - 4\lambda^2})}{\lambda|E^2 - J'^2 - 1| + \lambda\sqrt{(E^2 - J'^2 - 1)^2 - 4J'^2}} \right|, 0 \right\}, & |E| > 2\lambda \text{ \& } |E^2 - J'^2 - 1| > 2J', \\ \max \left\{ \ln \left| \frac{2J'}{|E^2 - J'^2 - 1| + \sqrt{(E^2 - J'^2 - 1)^2 - 4J'^2}} \right|, 0 \right\}, & |E| \leq 2\lambda \text{ \& } |E^2 - J'^2 - 1| > 2J', \\ \max \left\{ \ln \left| \frac{|E| + \sqrt{E^2 - 4\lambda^2}}{2\lambda} \right|, 0 \right\}, & |E| > 2\lambda \text{ \& } |E^2 - J'^2 - 1| \leq 2J', \\ 0, & |E| \leq 2\lambda \text{ \& } |E^2 - J'^2 - 1| \leq 2J'. \end{cases} \quad (\text{S69})$$

Similarly, since the second (third) line of inequality satisfies $|E^2 - J'^2 - 1| > 2J'$ ($|E| > 2\lambda$), we have $\gamma_K = 0$ ($\gamma_K > 0$). The final LE for dual space is

$$\gamma_K = \begin{cases} \max \left\{ \ln \left| \frac{J'(|E| + \sqrt{E^2 - 4\lambda^2})}{\lambda|E^2 - J'^2 - 1| + \lambda\sqrt{(E^2 - J'^2 - 1)^2 - 4J'^2}} \right|, 0 \right\}, & |E| > 2\lambda \text{ \& } |E^2 - J'^2 - 1| > 2J', \\ 0, & |E| \leq 2\lambda \text{ \& } |E^2 - J'^2 - 1| > 2J', \\ \ln \left| \frac{|E| + \sqrt{E^2 - 4\lambda^2}}{2\lambda} \right|, & |E| > 2\lambda \text{ \& } |E^2 - J'^2 - 1| \leq 2J', \\ 0, & |E| \leq 2\lambda \text{ \& } |E^2 - J'^2 - 1| \leq 2J'. \end{cases} \quad (\text{S70})$$

C. Mobility edge

Comparing the LE in the two dual spaces, one can find that the eigenstates in the region of $|E| \leq 2\lambda$ & $|E^2 - J'^2 - 1| \leq 2J'$ are delocalized in both spaces, which means they are actually the multifractal state. Moreover, the LE does not depend on the coupling parameter t . In other words, for arbitrarily small t , one can induce multifractal states in this lattice model. The ME between the extended and localized states is determined by the LE of the energy region with $|E| > 2\lambda$ & $|E^2 - J'^2 - 1| > 2J'$ for $E_c = \frac{J' \pm \sqrt{J'^2 + 4\lambda^2(J'^2 + 1)}}{2\lambda}$.

TABLE IV. MMEs and quantum phases of partially-quasiperiodic lieb lattice

Quasiperiodic strength	$\lambda < (J' + 1)/2$		$\lambda \geq (J' + 1)/2$
Exact MMEs ($E_c =$)	$\pm 2\lambda$	$\frac{J' \pm \sqrt{J'^2 + 4\lambda^2(J'^2 + 1)}}{2\lambda}$	± 2
Separated states	Ext.* and Mul.	Ext. and Loc.	Ext. and Mul.
Possible phases	Ext.+Loc., Ext+Mul.+Loc.		Loc.+Mul.

*Ext.=Extended states; Loc.=Localized states; Mul.=Multifractal states.

The LE versus E and λ is shown in Fig. S9(b).

In the first stage [$\lambda < (J' + 1)/2$], the system has four MEs. Two are $E_c = \pm\lambda$ separating the extended and the multifractal state, while the other two are $E = \frac{J' \pm \sqrt{J'^2 + 4\lambda^2(J'^2 + 1)}}{2\lambda}$ separating the extended and the localized state.

In other words, though MMEs separating multifractal and localized states are not found in the first stage, this does not mean that the three-state coexisting quantum phase can not appear. As shown in Fig. S9(c), the IPR reflects that near $\lambda = 0.7$, three-state coexisting quantum phase emerges.

In the second stage [$\lambda \geq (J' + 1)/2$], the region $-J' - 1 \leq \frac{J' \pm \sqrt{J'^2 + 4\lambda^2(J'^2 + 1)}}{2\lambda} \leq J' + 1$ no longer satisfies the energy interval in the first line of Eq. (S62) and (S70). As a result, the MEs separating the extended and localized states

disappear. At this point the system enters a quantum phase in which the multifractal and the localized state coexist, separated by MMEs of $E = \pm 2$.

Finally, we summarize the MMEs and emergent quantum phases of the partially-quasiperiodic Lieb lattice in Tab. IV. The results again reveal that the system contains not only the traditional ME separating extended and localized states, but also the MMEs separating multifractal and localized states or separating multifractal and extended states. Meanwhile, exotic quantum phases featuring two-state coexistence (Ext. + Loc. or Loc. + Mul.) and three-state coexistence (Ext. + Mul. + Loc.) emerge.

This is yet another evidence supporting the conclusion: The MMEs and exotic quantum phases can emerge in the flat-band system.

VI. EXPERIMENTAL SCHEME OF THE RYDBERG ATOMIC ARRAY

Experimentally, one can realize the MMEs in diamond flat-band model by the following spin Hamiltonian

$$H_s = \sum_{j_x} (J\sigma_{j_x,A}^+ \sigma_{j_x,B}^- + J\sigma_{j_x,A}^+ \sigma_{j_x,C}^- + t\sigma_{j_x,B}^+ \sigma_{j_x,C}^- + J\sigma_{j_x,B}^+ \sigma_{j_x+1,A}^- + J\sigma_{j_x,C}^+ \sigma_{j_x+1,A}^- + \text{H.c.}) + \frac{1}{2} \sum_{j_x} V_{j_x} (\mathbb{I} + \sigma_{j_x,C}^z). \quad (\text{S71})$$

This Hamiltonian can be transformed to the diamond quasiperiodic lattice by relabeling site index $j_x \rightarrow n$ for each leg and defining operator $b_n^\pm = |\uparrow\rangle_n \langle\downarrow|_n$ at each site. We consider the three-legged superarray of Rydberg atoms, and each atom is trapped in optical tweezers. The schematic diagram is shown in Fig. S10(a), where $R_1 = \frac{2R_y}{\sin \theta_A}$, $R_2 = \sqrt{R_1^2 + R_x^2 - 2R_1R_x \cos \theta_A}$, $R_3 = \sqrt{2R_1R_2 \cos(\theta_1 + \theta_2)}$. From the sine and cosine theorems, we can further give the angle between the sublattice $\theta_1 = \pi - \theta_m - \theta_A$, $\theta_2 = \theta_m - \arcsin(\frac{R_1}{R_2} \sin \theta_A)$ and $\theta_3 = \theta_m - \arcsin(\frac{2R_1}{R_3} \sin \theta_A)$, where $\theta_m = 54.7^\circ$ is the magic angle.

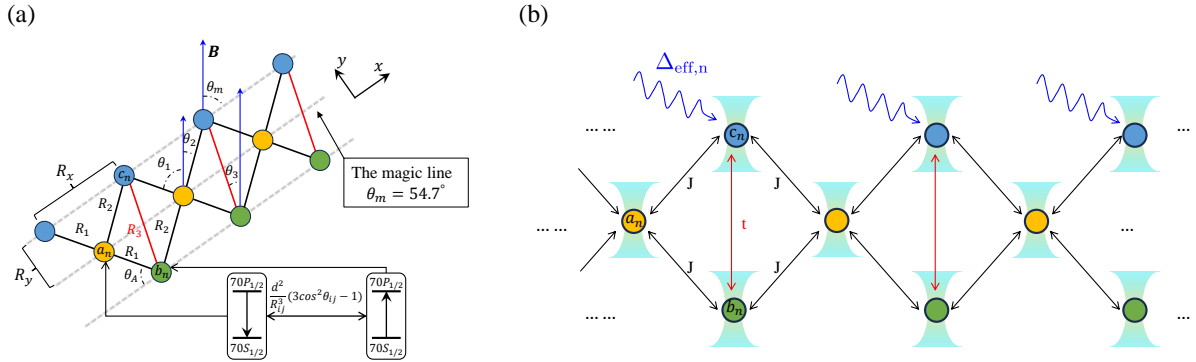


FIG. S10. Experimental scheme on MMEs of model (S7) in Rydberg atomic array. The corresponding angles are marked.

To realize the above Hamiltonian (S71) in Rydberg atomic array, angle-dependent dipole-dipole interactions and the AC Stark potential need to be realized successively, then the total Hamiltonian of the experimental system reads

$$H = H_{dipole} + H_{AC}(r), \quad (\text{S72})$$

where the AC Stark term reads

$$H_{AC} = \sum_{j_x} \frac{|\Omega_0|^2}{\Delta} \cos^2(2\pi\alpha j_x) (\mathbb{I} + \sigma_{j_x,C}^z), \quad (\text{S73})$$

and the dipole-dipole term reads

$$H_{dipole} = \sum_{j_x} (J_{AB}\sigma_{j_x,A}^+ \sigma_{j_x,B}^- + J_{AC}\sigma_{j_x,A}^+ \sigma_{j_x,C}^- + J_{BC}\sigma_{j_x,B}^+ \sigma_{j_x,C}^- + J_{BA}\sigma_{j_x,B}^+ \sigma_{j_x+1,A}^- + J_{CA}\sigma_{j_x,C}^+ \sigma_{j_x+1,A}^- + \text{H.c.}) + \sum_{|i-j|>1} (\frac{J_{ij}}{R_{ij}^3} \sigma_{i,A}^+ \sigma_{j,B}^- + \frac{J_{ij}}{R_{ij}^3} \sigma_{i,A}^+ \sigma_{j,C}^- + \frac{J_{ij}}{R_{ij}^3} \sigma_{i,B}^+ \sigma_{j,C}^- + \text{H.c.}). \quad (\text{S74})$$

Here $\sigma^\pm = \frac{1}{2}(\sigma_x \pm i\sigma_y)$, σ_x and σ_y are the Pauli matrices. The dipole-dipole interaction between Rydberg atoms is given by $J_{ij} = \frac{d^2}{R_{ij}^3}(3\cos^2\theta_{ij} - 1)$, where d represents the transition dipole moment between the two Rydberg levels, R_{ij} with $i, j = A, B, C$ is the distance between sites i and j , and θ_{ij} is the angle between R_{ij} and the quantization axis defined by the magnetic field \mathbf{B} [58]. J_{ii} can be effectively mitigated to zero by selecting the angle θ_{ii} to be the magic angle $\theta_m = 54.7^\circ$. Note that, the hopping term $J_{AB} = J_{AC} = J_{BA} = J_{CA} = J$ and $J_{BC} = t$, i.e., $\frac{d^2}{R_1^3}(3\cos^2\theta_1 - 1) = \frac{d^2}{R_2^3}(3\cos^2\theta_2 - 1) = J$ and $\frac{d^2}{R_3^3}(3\cos^2\theta_3 - 1) = t$. The non-nearest neighboring term can be safely ignored since its value decays with distance R_{ij}^3 . Then, by setting values of any two of θ_A , R_x and R_y , the value of the third can be readily obtained by expressions $\frac{d^2}{R_1^3}(3\cos^2\theta_1 - 1) = \frac{d^2}{R_2^3}(3\cos^2\theta_2 - 1)$. For example, if we give $\theta_A = 50^\circ$, $R_x = 0.5a$, we get $R_y = 0.652a$. Then we obtain $J \propto 3.59d^2$ and $t \propto 0.66d^2$. In this case, we have $t/J = 0.184$.

VII. THE MEASUREMENT SCHEME

VII-1. Basic principles

In this section, we discuss the measurement scheme of MMEs. We here address an experimentally feasible method to detect the IPRs and LEs based on a powerful spectroscopic approach outlined in Ref. [61].

According to the basic principles of quantum mechanics, the dynamics of a quantum system with time-independent Hamiltonian satisfies the Schrödinger equation. One can get the wave function versus time, i.e.,

$$|\psi(t)\rangle = e^{-iHt}|\psi(0)\rangle = \sum_{\beta} e^{-iHt}|\psi_{\beta}\rangle \langle\psi_{\beta}|\psi(0)\rangle = \sum_{\beta} C_{\beta} e^{-iE_{\beta}t} |\psi_{\beta}\rangle, \quad (\text{S75})$$

where $C_{\beta} = \langle\psi_{\beta}|\psi(0)\rangle$ and $\beta \in \{1, 2, 3, \dots, 3N\}$ corresponds to the eigenvalue index. One can obtain the expected value of an observable \hat{O} at time t as

$$O(t) = \langle\psi(t)|\hat{O}|\psi(t)\rangle = \sum_{\beta, \beta'} O_{\beta', \beta} C_{\beta} C_{\beta'}^* e^{-i(E_{\beta} - E_{\beta'})t}, \quad (\text{S76})$$

where $O_{\beta', \beta} = \langle\psi_{\beta'}|\hat{O}|\psi_{\beta}\rangle$. From the expression, one can find that to get the expected value of an observable, we need to measure the energy difference. Experimentally, we use the spectroscopic method proposed in Ref. [61] to extract the eigenvalues. In other words, what we want to measure is E_{β} rather than $E_{\beta} - E_{\beta'}$. This problem can be solved by fixing $E_{\beta'}$ and using it as a reference energy [61]. Specifically, since the manifold that contains the vacuum state is a manifold containing only one state, we can extract the eigenenergy E_{β} by choosing the superposition of the vacuum state and the single excited state as the initial state, i.e.,

$$|\psi(0)\rangle_m = |0\rangle_1 \cdots |0\rangle_{m-1} \left(\frac{|0\rangle_m + |1\rangle_m}{\sqrt{2}} \right) |0\rangle_{m+1} \cdots |0\rangle_{3N} = \frac{1}{\sqrt{2}} (|\text{Vac}\rangle + |\mathbf{1}_m\rangle), \quad (\text{S77})$$

where $|\text{Vac}\rangle$ is the vacuum state and $|\mathbf{1}_m\rangle$ is an excited state at the m -th site. Under such circumstances, the corresponding Eq. (S75) can be rewritten as

$$|\psi(t)\rangle_m = e^{-iHt} |\psi(0)\rangle_m = \frac{1}{\sqrt{2}} \left(|\text{Vac}\rangle + \sum_{\beta} C_{\beta, m} e^{-iE_{\beta}t} |\psi_{\beta}\rangle \right), \quad (\text{S78})$$

where $C_{\beta, m} = \langle\psi_{\beta}|\mathbf{1}_m\rangle$ and $|\psi_{\beta}\rangle$ is an eigenstate of a singly excited state with the eigenenergy E_{β} . To measure the eigenvalue E_{β} , we need to measure the evolution of $\langle\sigma_m^x\rangle$ and $\langle\sigma_m^y\rangle$ to construct the annihilation operator, i.e., $\langle\hat{a}\rangle = \langle\sigma_m^+\rangle$, where $\langle\sigma_m^+\rangle = \langle\sigma_m^x\rangle + i\langle\sigma_m^y\rangle$. Then, one can get the expected value of σ_m^+ , i.e.,

$$\langle\sigma_m^+\rangle = \frac{1}{2} \sum_{\beta} |C_{\beta, m}|^2 e^{-iE_{\beta}t}. \quad (\text{S79})$$

The complete basis vectors are formed by scanning the parameter m from 1 to $3N$, such that each eigenstate has an overlap with all the different single excited initial states. In turn, each single excited initial state can expand by the eigenstates' complete basis, the coefficient of which is the probability that the initial state projects on different eigenstates.

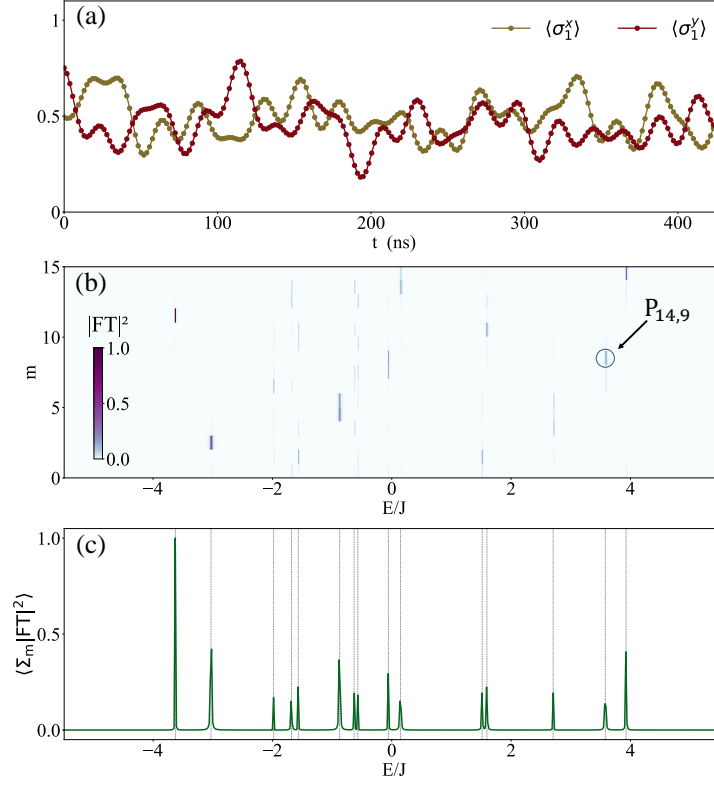


FIG. S11. (a) Typical data set showing $\langle \sigma_1^x \rangle$ and $\langle \sigma_1^y \rangle$ versus time. (b) The Fourier transformation (FT) of $\langle \sigma_m^+ \rangle$ curves. $m \in \{1, 2, \dots, 15\}$ correspond to different initial states. The probability of a single spin-flip state on the 9-th site in the 14-th eigenstate $P_{14,11}$ is highlighted. (c) Average $|\text{FT}|^2$ amplitudes of the data in (b). fifteen peaks emerge. Throughout, $J = 2\pi \times 7.53\text{MHz}$.

Note that, Eq. (S79) is structurally identical to the expression of discrete Fourier transform. Then, based on the similarity of the two, the eigenenergy and eigenstate can be extracted by Fourier transform (FT) from the evolution process. Specifically, the frequency in the Fourier transform expression corresponds to the eigenenergy $\{E_\beta\}$, and the amplitude of FT corresponds to $\{C_\beta\}$.

Now, we use a 5-unit-cell (15 Rydberg atoms) Rydberg atomic array as an example to briefly describe the measurement process. During the evolution process, one can obtain the time evolution curve of $\langle\sigma_m^x\rangle$ and $\langle\sigma_m^y\rangle$ [see Fig. S11(a)]. By conducting a Fourier transform on the evolution curve of $\langle\sigma_m^x\rangle$, one can obtain eigenenergy E_β and the corresponding modular square $|\text{FT}|^2$ on each site [see Fig. S11(a)], which can be defined as $P_{\beta,m}^R$ [see Fig. S11(b)]. In view of the correspondence relation between Eq. (S79) and the expression of Fourier transform, one can find that $P_{\beta,m}^R$ is actually the density distribution on m -th site. After obtaining all the $P_{\beta,m}^R$'s values, one can directly obtain the corresponding IPR ξ_R through the following relation

$$\xi_R(E_\beta) = \sum_n (P_{\beta,m}^R)^2. \quad (\text{S80})$$

Furthermore, by allowing such single site spin-flip to traverse the entire atomic chain from $m = 1$ to $m = 15$, one can experimentally extract all eigenvalues of the system [see Fig. S11(c)].

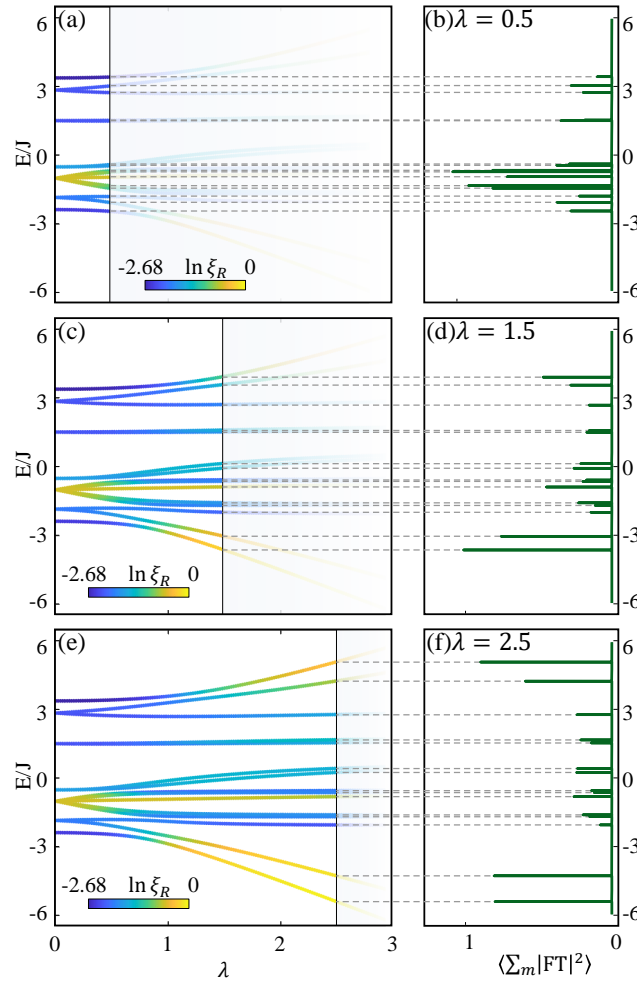


FIG. S12. The correspondence between the theoretically calculated eigenvalues (the left column) of different quasiperiodic strengths in the IPR diagram and the eigenvalues extracted from numerical simulated experiments (the right column). Throughout, $J = 2\pi \times 7.53\text{MHz}$.

By changing the quasiperiodic strength λ , we can obtain the phase diagram in lattice space. We numerically simulate the process of extracting IPR and draw the phase diagram. The results are plotted in Fig. S12 for the case of 5 unit cells. We compare the eigenenergy predicted by the theory (left column in Fig. S12) in the main text with

the eigenvalues extracted by the spectroscopic method for quasiperiodic strength $\lambda = 0.5, 1.5, 2.5$ (right column in Fig. S12). The results agree well with each other.

VII-2. The comparasion of IPRs obtained by the diagonalization and spectroscopic method

Fig. S13 compares the IPR results obtained by diagonalizing the Hamiltonian (S7) with those from the spectroscopic method of Ref. [61] under different unit cell sizes.

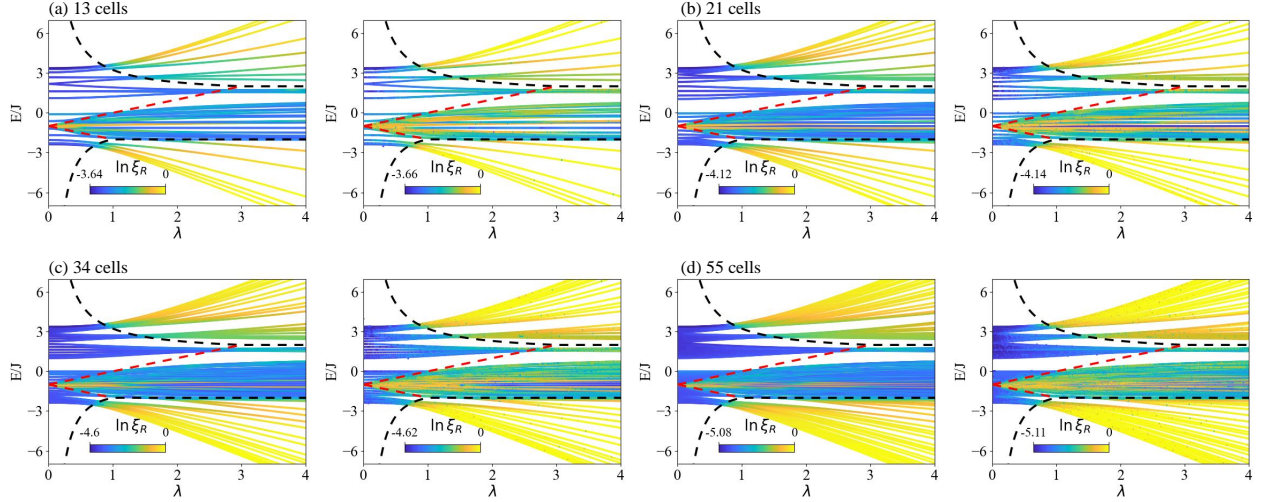


FIG. S13. Comparison of IPR between diagonalization calculation (the left column) and numerical simulated experiments (the right column) for the case of 13 (a), 21 (b), 34 (c), and 55 unit cells. Under the condition of the principal quantum number equals to 70, the energy unit $J = 2\pi \times 7.53\text{MHz}$.

The results reveal that 13-unit-cell systems capture the universal critical behavior predicted by our theory, confirming experimental feasibility with existing Rydberg array technologies. As for the corresponding dual space IPR phase diagram, one can obtain them by conducting a Fourier transform on the wave functions in real space. Then, based on the dual space wave function, we can obtain the corresponding dual sapce IPR.

VII-3. Scaling of IPRs in real and dual spaces

We exhibit the IPRs of $\lambda = 1.5$ for $N = 13, 21, 34, 55$ in the real space and dual space. As described in the main text, the key signatures are as follows: Localized/extended states: Real-space ξ_R and dual-space ξ_K IPRs exhibit spatial separation, with $\xi_R > \xi_K$ for localized states or $\xi_R < \xi_K$ for extended states. Multifractal states: ξ_R and ξ_K hybridize since $\xi_R \sim \xi_K$. One can find that 13-unit-cell system can capture key properties of MMEs.

VII-4. The corresponding LEs

A localized state wave function satisfies the expression

$$\psi_{R/K} \propto \max\{P_{\beta,m}^{R/K}\} e^{-\gamma_{R/K}(m-m_0)}, \quad (\text{S81})$$

where $\max\{P_{\beta,m}^{R/K}\}$ is the maximum amplitude with a fixed E_β . m_0 is the site index of the location of maximum amplitude. LE ($\gamma_{R/K}$) is another quantity to characterize the three phases and phase boundaries. From the results of $P_{\beta,m}^{R/K}$, one can directly obtain the corresponding eigenstates, and then by fitting the eigenstate exponentially, one can obtain the corresponding LEs.

One can select an arbitrary point with fixed disorder strength λ and energy parameters E/J in the localized phase region, where the corresponding eigenstates will exhibit localization properties ($\gamma_R > 0$) in real space and

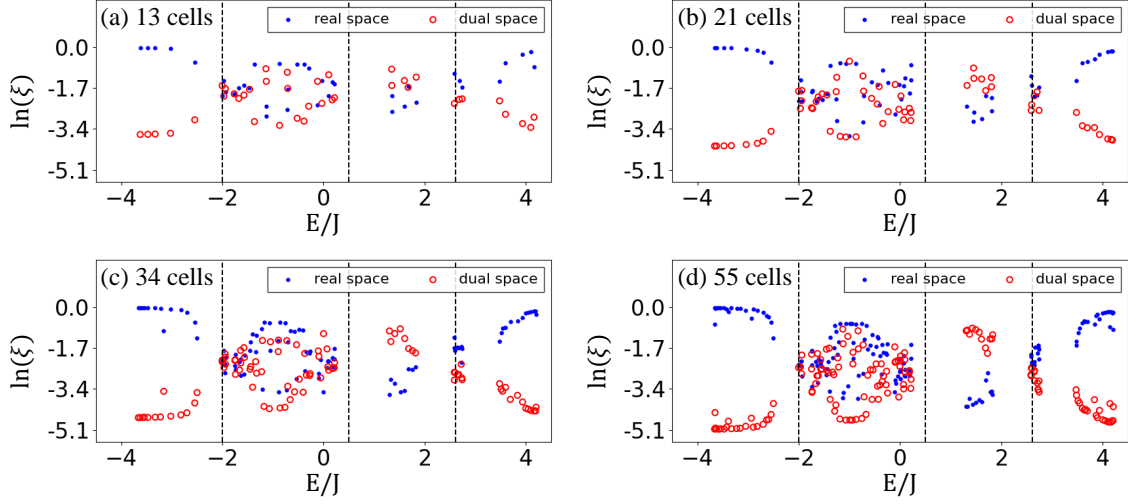


FIG. S14. The expected experimental IPRs for 13 (a), 21 (b), 34 (c) and 55 (d) cells. The lattice space IPR ξ_R and the dual space IPR ξ_K as functions of energy E/J

extension properties ($\gamma_K \approx 0$) in dual space. Similarly, wave function in the extended phase shows the extension property ($\gamma_K \approx 0$) in real space and the localization property in dual space ($\gamma_K > 0$). Multifractal states are in between ($\gamma_R \approx 0, \gamma_K \approx 0$). We can perform exponential fitting on the eigenstate wave functions extracted through spectroscopic techniques, thereby obtaining the corresponding expected experiment LEs. Then, based on the above criteria, one can determine the properties of different phase regions. The typical data are provided (see Fig. S15).

As shown in Fig. S15, selecting three parameter points (triangle, star, square) in three phase regions, one can obtain wave functions of extended, multifractal and localized states, respectively. Through the characteristics of both real and dual-space LEs, one can effectively distinguish three different phases.

VII-5. Self-similarity of multifractal states

The wave function with multifractal structure is self-similar. To demonstrate its self-similarity, here in Figure S16, we plot cases with the unit cell number $N = 13$ (a), $N = 55$ (b), $N = 89$ (c), and $N = 377$ (d). Self-similarity begins to emerge at system sizes $N=13$ and 55, and becomes much more pronounced at larger N values such as 89 and 377.

Summary. We propose the experimental implementation and measurement schemes based on the Rydberg atomic array platform. Specifically, we demonstrate a spectroscopic technique capable of measuring IPRs across real-space and dual-space (see Fig. S13 and Fig. S14). Based on this, we provide unambiguous criteria for determining different phase regions (Extended states: $\xi_R < \xi_K$; Localized states: $\xi_R > \xi_K$; Multifractal states: ξ_R and ξ_K hybridize since $\xi_R \sim \xi_K$), which are in good agreement with the phase boundary determined by the analytical solution. Furthermore, through this spectroscopic technique, we can also obtain the eigenstates' information. Then, LEs can be extracted through exponential fitting, so as to double check different phases and phase boundaries, i.e., Extended states: $\gamma_R \approx 0$ and $\gamma_K > 0$; Localized states: $\gamma_R > 0$ and $\gamma_K \approx 0$; Multifractal states: $\gamma_R \approx 0$ and $\gamma_K \approx 0$ (see Fig. S15). Finally, although this manuscript confirms that the MMEs and the three-state-coexisting quantum phase predicted by our theory can be experimentally verified through 13-unit-cell (tens of qubits), however, a larger size can no doubt better demonstrate the self-similarity of the multifractal wave function (see Fig. S16).

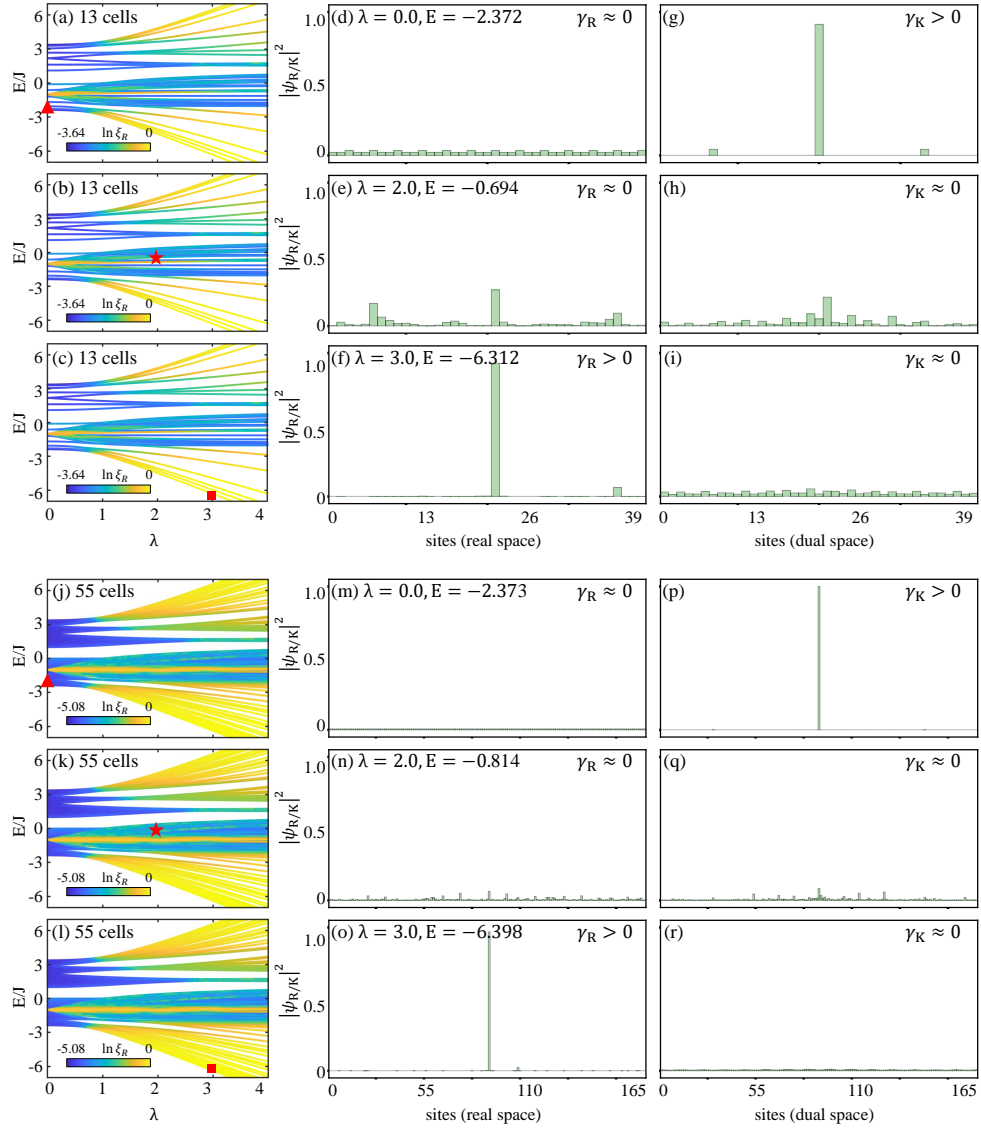


FIG. S15. The expected experiments LEs with 13 (a-i) and 55 (j-r) unit cells. From top to bottom, the results correspond to the cases of extended, multifractal and localized states, respectively. Throughout, $J = 2\pi \times 7.53\text{MHz}$.

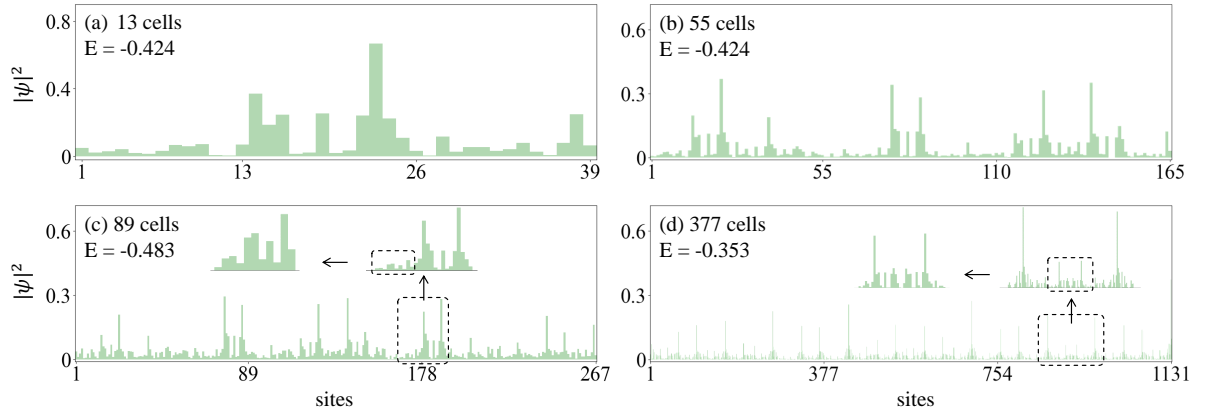


FIG. S16. Self-similar structure of multifractal wave functions with a fixed $\lambda = 2$. The number of unit cells are marked.